

## 8. TAG-2 AREA<sup>1</sup>

### Shipboard Scientific Party<sup>2</sup>

#### HOLE 957A

**Date occupied:** 5 October 1994  
**Date departed:** 7 October 1994  
**Time on hole:** 1 day, 1 hr, 30 min  
**Position:** 26°8.196'N, 44°49.552'W  
**Bottom felt (drill-pipe measurement from rig floor, m):** 3653.2  
**Distance between rig floor and sea level (m):** 11.29  
**Water depth (drill-pipe measurement from sea level, m):** 3641.9  
**Total depth (from rig floor, m):** 3668.2  
**Penetration (m):** 15.0  
**Number of cores (including cores having no recovery):** 3  
**Total length of cored section (m):** 15.0  
**Total core recovered (m):** 0.25  
**Core recovery (%):** 1.7  
**Hard rock:**  
Depth (mbsf): 15.0  
Nature: Sulfide breccia  
**Comments:** Test hole for HRB suitability

#### HOLE 957B

**Date occupied:** 7 October 1994  
**Date departed:** 10 October 1994  
**Time on hole:** 3 days, 15 min  
**Position:** 26°8.193'N, 44°49.546'W  
**Bottom felt (drill-pipe measurement from rig floor, m):** 3653.2  
**Distance between rig floor and sea level (m):** 11.32  
**Water depth (drill-pipe measurement from sea level, m):** 3649.1  
**Total depth (from rig floor, m):** 3682.8  
**Penetration (m):** 29.6  
**Number of cores (including cores having no recovery):** 5  
**Total length of cored section (m):** 29.6  
**Total core recovered (m):** 1.66  
**Core recovery (%):** 5.6

#### Hard rock:

Depth (mbsf): 29.6  
Nature: Sulfide breccia, basalt

#### Basement:

Depth (mbsf): 19.9  
Nature: basalt

**Comments:** Guide base placed; hole terminated after encountering fresh basalt

#### HOLE 957H

**Date occupied:** 27 October 1994  
**Date departed:** 30 October 1994  
**Time on hole:** 2 days, 15 hr, 30 min  
**Position:** 26°8.195'N, 44°49.555'W  
**Bottom felt (drill-pipe measurement from rig floor, m):** 3655.0  
**Distance between rig floor and sea level (m):** 11.63  
**Water depth (drill-pipe measurement from sea level, m):** 3643.4  
**Total depth (from rig floor, m):** 3709.5  
**Penetration (m):** 54.5  
**Number of cores (including cores having no recovery):** 9  
**Total length of cored section (m):** 45.8  
**Total core recovered (m):** 5.01  
**Core recovery (%):** 10.9  
**Hard rock:**  
Depth (mbsf): 54.5  
Nature: Massive pyrite and sulfide breccias, silicified basalt  
**Comments:** Drilled 0-8.7 mbsf

#### HOLE 957N

**Date occupied:** 10 November 1994  
**Date departed:** 12 November 1994  
**Time on hole:** 2 days, 3 hr, 30 min  
**Position:** 26°8.197'N, 44°49.553'W  
**Bottom felt (drill-pipe measurement from rig floor, m):** 3648.0  
**Distance between rig floor and sea level (m):** 11.87  
**Water depth (drill-pipe measurement from sea level, m):** 3636.1  
**Total depth (from rig floor, m):** 3690.2  
**Penetration (m):** 42  
**Number of cores (including cores having no recovery):** 1  
**Total length of cored section (m):** 42.2

<sup>1</sup>Humphris, S.E., Herzig, P.M., Miller, D.J., et al., 1996. *Proc. ODP, Init. Repts.*, 158: College Station, TX (Ocean Drilling Program).

<sup>2</sup>Shipboard Scientific Party is as given in the list of participants in the contents.

**Total core recovered (m):** 0.50 (wash core)

**Core recovery (%):** 1

**Hard rock:**

Depth (mbsf): 42.2

Nature: Massive sulfide, chert, and pyrite-silica breccia

**Comments:** Only wash core recovered

**Principal results:** Holes 957A, 957B, 957H, and 957N are located on the lower terrace of the active TAG mound in an area of white smoker chimneys (the Kremlin, or TAG-2, area). Objectives of drilling at this location were to sample a section of the mound where discharging fluids have undergone conductive cooling and mixing within the mound, resulting in chemistries distinct from those of the black smokers.

The holes were drilled in water depths of 3651–3655 m and were located within about 10–15 m of each other. The most complete section cored was Hole 957H (from 8.7 to 54.3 mbsf) with a recovery of 11.0%. Hole 957A was located about 5 m northwest of Hole 957H; it sampled the upper 15.0 m with recovery of 1.7%. Hole 957B was cored with recovery of 5% to a depth of 29.6 m about 8–10 m southeast of Hole 957H. It recovered a thick section of massive sulfides and penetrated 10–20 m into inferred basement. A single wash core covering the interval 0–42.2 mbsf was recovered from Hole 957N to the west of Hole 957A.

The stratigraphy of the sulfide section in the Kremlin area is similar for all the holes down to about 20 m. Drill cuttings from the very top of the section at Hole 957B consist of red-brown, sulfide-rich sand and mud with abundant chert clasts and a few small pieces of porous massive sphalerite and massive granular pyrite. The sulfide-rich sand and mud contains up to 16 wt% combined Cu and Zn (1–3 wt% Zn and 8–13 wt% Cu). A hard layer in the top few meters of each hole at TAG-2 consists of mixed pyrite and chert clasts in a dominantly cherty matrix. Clasts of similar red and gray chert are also common in the underlying massive, porous pyrite to a depth of about 10 mbsf.

Most of the sulfide material recovered from the TAG-2 area occurs in the upper 20 m of the section as massive porous pyrite and porous, nodular pyrite breccias. The more limited range of breccia types at TAG-2, compared with TAG-1 and TAG-4, implies a different history of brecciation, cementation, and veining. The upper 10 m of the core in Holes 957A and 957H consists of massive, porous to granular pyrite with abundant red and gray chert. The massive pyrite is colloform banded and exhibits primary depositional textures, with only limited replacement and local recrystallization to coarse, granular pyrite. Between 10 and 20 mbsf, a zone of massive, nodular pyrite breccias containing rounded clasts of pyrite in a sandy pyrite matrix is present. Although the breccias are dominantly matrix supported, they contain only minor anhydrite cement.

Pyrite accounts for 80–90 vol% of the rock in the upper 20 m, and chalcopyrite is locally abundant in the upper 15 m of the core as disseminated grains and clasts in the sandy pyrite matrix, replacing the colloform pyrite and locally associated with anhydrite veins. Sphalerite occurs mainly as coatings on massive colloform pyrite and in late cavities or fluid channelways in the upper 5 m of core. A sample of nodular, pyrite breccia from about 10 mbsf contains close to 7 wt% Cu. Zinc contents are low in samples from Hole 957H below about 8 mbsf (<0.02 wt% compared with 1–3 wt%).

Between 20 and 30 mbsf in Hole 957H, massive pyrite breccias grade into pyrite-silica breccias, which consist of nodular clasts of quartz and pyrite in a quartz-rich matrix with anhydrite veining. Silicified wallrock fragments and altered hyaloclastite first occur at a depth of 27 mbsf, and the wallrock fragments become increasingly abundant deeper in the core. Below 27 mbsf, the fragments in the pyrite-silica breccias become coarser and more angular and are interspersed with sections of brecciated and silicified wallrock. At about 40 mbsf, the pyrite-silica breccias grade into more massive silicified wallrock breccias, and chloritized basalt fragments are present locally among the clasts. The silicified wallrock breccias represent the upper part of the stockwork zone below the massive sulfides. This stratigraphic sequence suggests that the thickness of the sulfide mound beneath the Kremlin area is only about 25 m.

The silicified basalt clasts in the pyrite-silica breccias of Holes 957H and 957N, and in the silicified wallrock breccias of Hole 957H, are gray to buff, 2 mm to 3 cm, rounded to angular fragments in a fine-grained matrix of gray quartz plus pyrite. Pyrite in the matrix is present as 0.1- to 1-cm grains and rounded aggregates. The basalt clasts themselves are composed of a buff phyllosilicate plus quartz, and they contain variable amounts of fine-grained pyrite replacing plagioclase microlites and disseminated in the groundmass. The clasts are replaced by quartz to varying extent, with gray portions that are more intensively silicified. The silicified hyaloclastite from Hole 957H consists of 1- to 5-mm, angular fragments of altered basaltic glass in a matrix of fine-grained gray quartz. The glass fragments are altered to green chlorite and a white phyllosilicate, commonly in concentric bands. The glass shards are also variably silicified and replaced by fine-grained pyrite.

Anhydrite veins are less abundant in rocks recovered from the TAG-2 area than in rocks recovered from the TAG-1 area. Late anhydrite veins, up to several centimeters in width, occur in the pyrite-silica breccias in Hole 957H. Quartz veining is abundant in pyrite-silica breccias below the massive sulfides, and small quartz-pyrite veins (up to 1 cm) are the dominant vein type in the silicified wallrock breccias to a depth of 45 mbsf.

In Hole 957B, massive porous pyrite and pyrite breccias, similar in texture and mineralogy to those observed in Hole 957H, are present to a depth of about 20 mbsf. At the base of the massive sulfides in Hole 957B, a 30-cm section of pillow rim breccia was recovered, which overlies partly altered basalt. This is interpreted to be the uppermost basement or a portion of a basaltic flow. Centimeter-sized pieces of altered crystalline and glassy basalt occur in a matrix of red chlorite + hematite + quartz mud. The crystalline basalt fragments are grayish red and completely replaced by yellow phyllosilicates (smectite?) and Fe-oxides and/or oxyhydroxides. Basaltic glass fragments are blue and completely altered to chlorite. The strongly altered pillow-rim breccia at the contact between relatively fresh basalt and the base of the massive sulfides indicates local hydrothermal flow along the contact at the base of the sulfide breccias.

Fragments of red brown to dark gray, very fine-grained aphyric to sparsely phyrlic basalt occur in the lowermost portion of Hole 957B. They exhibit rare olivine phenocrysts in a microcrystalline groundmass containing plagioclase microlites. Furthermore, they are slightly altered with olivine phenocrysts replaced by smectite and iron oxyhydroxides and/or oxides. Small rounded to elongated vesicles make up 1%–2% of these samples.

Physical properties of sulfide specimens from the Kremlin area yielded a range of bulk densities from 2.61 to 4.33 g/cm<sup>3</sup> and porosities between 6.38% and 21.5%. Electrical resistivity values measured on two sulfide minicores are low (0.07 and 0.58 Ωm). Compressional (*P*-wave) velocities of minicores vary from 5.4 to 6.7 km/s, and thermal conductivities from 8.0 to 10.4 W/(m·K). Two altered basalt samples have high porosities (15.7% and 18.6%) and low wet bulk densities (2.25 and 2.43 g/cm<sup>3</sup>), reflecting their altered character.

The rocks recovered from Hole 957H displayed a multicomponent magnetization. The unstable viscous component is characterized by higher magnetic susceptibility and a lower Koenigsberger ratio. This viscous magnetization can be removed by AF demagnetization. The downhole magnetic profile shows a trend of increasing intensity with depth, which coincides with the observed changes in lithology. No noticeable magnetic anisotropies were observed.

## STRATIGRAPHY

### Introduction

Holes 957A, 957B, and 957H in the TAG-2 area are located on the lower terrace of the mound, within about 10 m of each other in the Kremlin white smoker field (see Fig. 3, Chapter 1, this volume). This area is about 60 m southeast of the Black Smoker Complex and about 20 m from the eastern edge of the mound. The holes were drilled in water depths of 3651–3655 m and penetrated to a maximum depth of 55 mbsf. The most complete section of stratigraphy through this part

**Table 1. Distribution of dominant lithologies in core from the TAG-2 area.**

Dominant lithology	Intervals recovered	Approximate location		Estimated total thickness (m)	
		Top (mbsf)	Bottom (mbsf)		
Surface material	158-957B-1R-1	(0–1.0 m)	0	1.0	1.7
	158-957B-1R-2	(0–0.1 m)	—	1.7	
Porous, massive pyrite (Type 5) with red and gray chert	158-957A-1X-1	(0–0.1 m)	0	0.1	10
	158-957A-2X-1	(0–0.02 m)	5.0	5.0	
	158-957A-3X-1	(0–0.6 m)	10.0	10.6	
	158-957H-1N-1	(0–0.5 m)	8.7	9.2	
	158-957B-1R-2	(0–0.2 m)	1.1	1.2	
Massive pyrite breccias (Type 6)	158-957H-1N-1	(0.5–0.9 m)	9.2	9.6	10
	158-957H-2N-1	(0–0.2 m)	13.2	13.4	
	158-957H-3N-1	(0–0.8 m)	17.7	18.5	
	158-957B-3R-1	(0–0.1 m)	14.9	—	
Pyrite-silica breccias (Type 9) with anhydrite veins	158-957H-5N-1	(0–0.9 m)	26.7	27.6	10
Pyrite-silica breccias (Types 9) with silicified wallrock	158-957H-5N-2	(0–0.8 m)	27.6	28.4	15
	158-957H-6N-1	(0–0.4 m)	31.2	31.6	
	158-957H-7N-1	(0–0.1 m)	35.7	35.8	
	158-957H-8N-1	(0–1.1 m)	40.2	41.3	
Silicified wallrock breccias (Type 10a)	158-957H-9X-1	(0–0.1 m)	44.7	44.8	—
Clay horizon	158-957B-4R-1	(0–0.4 m)	19.9	20.3	1
Weakly altered basalt	158-957B-4R-1	(0–0.5 m)	20.3	20.4	—
	158-957B-5B-1	(0–0.04 m)	—	29.6	

of the mound was cored in Hole 957H (from 9 to 55 mbsf), with a recovery of about 11%. Hole 957A was cored to a depth of about 15 m, with a recovery of 1.7%, and sampled the upper few meters of the mound next to Hole 957H. Hole 957B was cored to a depth of nearly 30 m, with a recovery of 5.5%. This hole sampled a thick section of massive sulfides and penetrated 10–20 m into inferred basement near the edge of the lower terrace, about 10 m southeast of Hole 957H. Graphic logs of the most complete core sections are shown in Figure 1, and Table 1 lists the different rock types and their distribution in each core. For more detailed descriptions of the rock types encountered in the TAG-2 area, see the “Sulfide Petrology and Geochemistry” section (this chapter).

In general, the TAG-2 area does not exhibit such a wide variety of breccias and styles of brecciation as observed in either the TAG-1 or TAG-4 area. This most likely reflects a different history of brecciation, cementation, and veining in the TAG-2 area. The upper part of the core in Holes 957A and 957H, to a depth of approximately 10 mbsf, consists of massive, porous pyrite with abundant red and gray chert. This material is underlain by a 10-m-thick zone of massive pyrite breccias followed by pyrite-silica breccias with anhydrite veining. Below about 30 mbsf, the pyrite-silica breccias contain numerous silicified wallrock fragments, and these increase in abundance to a depth of about 40 mbsf, where silicified wallrock breccias are the dominant lithology. In adjacent Hole 957B, massive porous pyrite and pyrite breccias are present to a depth of about 20 mbsf, where they are in contact with hydrothermally altered basalt breccia overlying slightly altered basalt.

### Distribution of Lithologies

Drill cuttings from the very top of the mound in Core 158-957B-1R consist of red-brown, sulfide-rich sand and mud with abundant chert clasts. The sulfide component of this material may represent near-surface hydrothermal precipitates similar to those observed in cores from Hole 957F. A hard layer in the top few meters of each hole consists of mixed pyrite and chert clasts in a dominantly cherty matrix. Clasts of similar red and gray chert are also common in the underlying massive, porous pyrite to a depth of about 10 mbsf. The massive pyrite is colloform banded and exhibits primary depositional textures, with only limited replacement and local recrystallization to

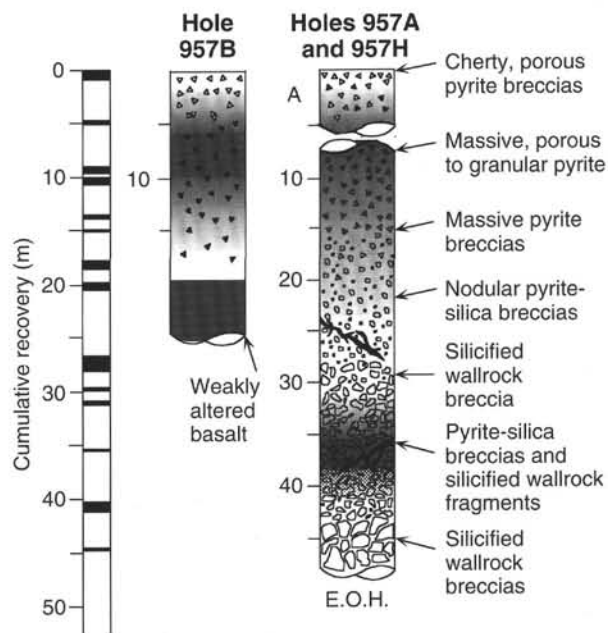


Figure 1. Schematic stratigraphic section of the mound in the TAG-2 area showing cumulative recovery and the distribution of the principal rock types in cores from Holes 957A, 957B, and 957H. E.O.H. = end of hole.

coarse, granular pyrite. Sphalerite is present locally as overgrowths on the colloform pyrite and filling late cavities. Between 10 and 20 mbsf, the bulk of the massive sulfide consists of nodular pyrite breccias containing rounded clasts of pyrite in a sandy pyrite matrix. Although the breccias are dominantly matrix supported, they contain only minor anhydrite cement. Between 20 and 30 mbsf, the massive pyrite breccias grade into pyrite-silica breccias consisting of nodular clasts of quartz and pyrite in a quartz-rich matrix. These rocks resemble the upper part of the quartz-rich stockwork in the TAG-1 area, suggesting that the thickness of the sulfide mound beneath the Krem-

lin area is only about 25 m. Silicified wallrock fragments and altered hyaloclastite first occur in Section 158-957H-5N-1 at a depth of 27 mbsf, and the wallrock fragments become increasingly abundant deeper in the core. Below 27 mbsf, the pyrite-silica breccias become coarser and more angular and are interspersed with brecciated and silicified wallrock. At about 40 mbsf, the pyrite-silica breccias grade into more massive silicified wallrock breccias, and chloritized basalt fragments are present locally among the clasts.

At the base of the massive sulfides in Hole 957B, a thin (<1 m), clay-rich horizon of hematitized basalt and chloritized pillow-rim breccia occurs on top of weakly altered basalt. This is interpreted to be the uppermost basement or a portion of a basaltic flow and suggests that the mound may be only 20 m thick at the eastern edge of the lower terrace. The strongly altered (chloritized) contact between relatively fresh basalt breccias and the base of the massive sulfides may indicate local hydrothermal flow along the contact of the basalts at the base of the sulfide breccias (see "Hydrothermal Alteration" section, this chapter). The depth to the top of the quartz-pyrite stockwork in Hole 957H is at least 5 m below the basalt in Hole 957B and may indicate displacement of the footwall along a fault scarp.

### Veining

Anhydrite veins are less abundant in the rocks recovered from the TAG-2 area than in the rocks recovered from the TAG-1 area, and anhydrite-bearing breccias occur only in the upper 20 m of massive sulfide and sulfide breccias. Anhydrite accounts for only 10 vol% of the recovered rock in this part of the mound. Late anhydrite veins, up to several centimeters in width, occur in the pyrite-silica breccias (Section 158-957H-5N-1) at about the same depth as the anhydrite-rich zone in the TAG-1 area (see "Stratigraphy" section, Chapter 7, this volume). Quartz veining is abundant in pyrite-silica breccias below the massive sulfides, and small quartz-pyrite veins (up to 1 cm) are the dominant vein type in the silicified wallrock breccias to the maximum depth cored (45 mbsf).

### Mineralization

Most of the sulfides in the TAG-2 area occur in massive porous pyrite and porous, nodular pyrite breccias near the top of the mound. Pyrite accounts for 80–90 vol% of the rock recovered in the upper 20 m, and chalcopyrite is locally abundant in the upper 15 m of the core, as disseminated grains and clasts in the sandy pyrite matrix, replacing the colloform pyrite, and locally associated with anhydrite veins. Sphalerite occurs mainly as coatings on massive colloform pyrite and in late cavities or fluid channelways in the upper 5 m of core. Surface material recovered as drill cuttings in core from Hole 957B contains up to 17 wt% combined Cu and Zn (1–3 wt% Zn and 8–13 wt% Cu); a sample of nodular, pyrite breccia from about 10 mbsf contains close to 7 wt% Cu. Zn contents are below detection in samples from Hole 957H below about 8 mbsf. Abundant quartz-pyrite mineralization and quartz veining occurs immediately beneath the massive sulfides, within the pyrite-silica breccias, and near the top of the silicified wallrock breccias. These rocks contain 40–50 vol% quartz with 50–60 vol% pyrite disseminated throughout the clasts and matrix and in quartz-pyrite veins.

### Interpretation

The section of core from the TAG-2 area indicates that the sulfides at the eastern edge of the lower terrace are 20 m thick. The sulfide breccias are either clast supported or set in a matrix of fine-grained detrital sulfides, containing abundant sand-sized pyrite and chalcopyrite. This material was presumably derived from the erosion of sulfide chimneys on top of a former mound/stockwork complex. The breccias exhibit only minor replacement, veining, and cementation by quartz and anhydrite. In the Kremlin area, the upper 10 m of the mound consists of massive colloform pyrite with minor late

sphalerite lining cavities and fluid channelways. This sphalerite is probably related to the current white smoker activity at the surface of the mound. Massive, nodular pyrite breccias beneath the Kremlin area may represent an earlier generation of sulfide talus that was accumulated on the eastern flanks of the growing sulfide mound. Alternatively, they may have formed locally from the collapse of hydrothermal material deposited at the surface (as at TAG-1). The presence of abundant chert clasts also suggests local brecciation and erosion of the upper cherty layer of the mound during its growth, although some clasts deeper in the mound appear to be remnants of inter-pillow cherts.

Pyrite-silica breccias at the base of the massive sulfide section (20–25 mbsf) contain abundant partially replaced wallrock fragments in a matrix of pyrite and lesser quartz. However, many of the original wallrock fragments are intact and do not appear to have experienced the same wholesale replacement by quartz exhibited by breccias in the TAG-1 area, closer to the main upflow zone. The absence of altered basalt clasts in the upper 25 m of core suggests that most of the wallrock fragments in the pyrite-silica breccias could have been derived from a now-buried fault scarp to the east of Hole 957H (i.e., between Holes 957H and 957B). Although a portion of the quartz-pyrite stockwork was intersected below about 30 mbsf in Hole 957H, the extent of the stockwork zone beneath the TAG-2 area could not be determined. The presence of chloritized basalt fragments in the lower part of the core suggests proximity to a chloritic alteration zone at depth or at the outer margins of the quartz stockwork. In addition, the relatively fresh basaltic basement in core from Hole 957B suggests that the outer limit of the stockwork zone is immediately to the east of Hole 957H and likely dips steeply toward the center of the mound. The submound stratigraphy at the edge of the lower terrace may be part of a recent lava flow or, more likely, has been isolated from prolonged hydrothermal alteration during the growth of the mound. An apparent offset in the depth to basement in these cores suggests that the stockwork zone may be fault controlled.

## SULFIDE PETROLOGY AND GEOCHEMISTRY

### Introduction

Holes 957A, 957B, 957H, and 957N are located in the southeast quadrant of the active TAG mound, in an area of white smoker chimneys (the Kremlin, or TAG-2, area; see Fig. 3, Chapter 1, this volume). Precipitates recovered in Hole 957A, which was drilled to a total depth of 15 mbsf with recovery of 1.7%, include Fe-oxide (Type 1), siliceous material (red chert [Type 2], gray silica [Type 3], chert-sulfide breccia [Type 4]), massive sulfide (porous massive pyrite [Type 5a] and porous massive sphalerite [Type 5b]). Hole 957B, located 15–20 m southeast of Hole 957A, penetrated 29.6 m of hydrothermal oxides (in drill cuttings), massive sulfide (porous massive sphalerite [Type 5b], massive granular pyrite [Type 5c], and silica (red and gray chert [Type 2]), into altered basalt. Recovery was 5.5%. Hole 957H is located approximately 5 m southeast of Hole 957A. It was drilled to a depth of 8.7 mbsf without recovery and cored to a depth of 54.5 mbsf until hole instability and fill problems caused it to be abandoned. Overall recovery was 10.9%. Samples recovered between depths of 8.7 and 31.2 mbsf supplement samples recovered in Holes 957A and 957B. Rock types recovered from Hole 957H include gray and red chert (Type 2), porous massive pyrite (Type 5a), massive granular pyrite (Type 5c), massive pyrite breccia (Type 6), porous nodular pyrite breccia (Type 6a), pyrite-silica breccia (Type 9a), nodular pyrite-silica breccia (Type 9b), and silicified wallrock breccia (Type 10a). Hole 957N was located 5 m west of Hole 957A. A single wash core (Core 158-957N-1W) recovered pieces of red and gray chert (Type 2), pyrite-silica-anhydrite breccia (Type 8), and nodular pyrite-silica breccia (Type 9b).

This section describes the mineralogy, chemical composition, textural features, and mode of occurrence of the different types of hydrothermal precipitates recovered from the TAG-2, or Kremlin, area.

Table 3. Structural log.

Core, section, interval (cm)	Piece no.	Curatorial depth (cm)	Estimated depth (mbsf)	Identifier	ID no. in SVCD	Min. thickness (mm)	Max. thickness (mm)	Est. thickness (mm)	Est. thickness (mm)	App. dip dir. 1	App. dip dir. 2	Strike	Dip dir.	Dip	Comments
158-957A-3X-1, 8-13	2	10	10.1			0.2	2								Irregular network, 0.2-2 mm width fractures in red silica Irregular network, 0.2-2 mm width fractures in red silica
3X-1, 13-18	3	16	10.2			0.2	2								
158-967H-5N-1, 52-54	5B	53	27.2	Vh	v1	3	6	5	5	270	0	180	270	41	
5N-1, 58-59	5C	59	27.3	Vh	v2	3	3	3	270	19	0	180	270	19	
5N-1, 68-77	7	73	27.4	Vh	v3	2	5	4	90	78	0	257	347	78	
5N-2, 38-39	ID-E	39	28	Vh	v1	1	1	1	270	21	0	180	270	21	
5N-2, 44-46	1E	45	28.1	Vh	v2	5	1	5	270	64	0	180	270	64	

Drill cuttings from Hole 957B, and three samples of material recovered from Hole 957H (one porous nodular pyrite breccia, and two nodular pyrite-silica breccias) were analyzed by AAS and CHNS for Fe, Zn, Cu, Pb, Ag, Cd, and S. Listings of the visual core descriptions and structural descriptions are given in Table 2 (in back pocket) and in Table 3. A schematic stratigraphic section of the holes is illustrated in Figure 1. Figures 2 and 3 are detailed logs of the cores. Rock types recovered from the TAG-2 area are described below.

### Hole 957A

Hydrothermal precipitates were recovered in three cores from Hole 957A. Two samples of porous massive pyrite, and one sample of red chert were recovered from the depth interval 0-10 mbsf (Core 158-957A-1X). The second core (158-957A-2X) recovered a single small (3 cm) piece of Fe-oxide. Multiple pieces of porous massive pyrite and red chert, a single piece of chert-sulfide breccia, and several small (<2 cm) pieces of porous massive sphalerite were recovered in the third core (Core 158-957A-3X) from the depth interval at 10-15 mbsf.

#### Iron Oxide (Type 1)

Core 158-957A-2X recovered only one small piece of porous iron oxide (Type 1). This sample is comprised of orange-brown iron oxide and a 5-mm rim of porous gray silica.

#### Red and Gray Chert (Type 2)

Significant amounts of red and gray chert (Type 2) were recovered in Cores 158-957A-1X and 3X (Fig. 4). Disseminated fine to medium grains of pyrite, and locally of chalcopyrite, are present in the red chert at up to 20 vol% in a matrix of chalcedony stained red by Fe-oxides or oxyhydroxides. In polished thin section, chalcedony occurs as cryptocrystalline aggregates, Fe-oxides are present as amorphous aggregates, and pyrite occurs as anhedral to euhedral grains (Fig. 5). Fine-grained silica replaces Fe-oxides and pyrite, and minor late pyrite and sphalerite fill or line small void spaces. The red chert samples in Core 158-957A-3X exhibit open fractures <0.2 to 2 mm wide, variably filled by colorless silica, fine granular pyrite, euhedral quartz, and euhedral anhydrite. Anhydrite is also present and intermixed with fine-grained sulfide on the outer surfaces of these samples.

#### Gray Silica (Type 3)

One piece of gray silica (Type 3), which is comprised of 90% amorphous silica with variable amounts of disseminated fine-grained pyrite and minor sphalerite and chalcopyrite (Fig. 6), was recovered in Core 158-957A-3X. In polished thin section, pyrite occurs as fine euhedral grains, or as irregular colloform aggregates, and grains are locally corroded and replaced by silica. A second generation of pyrite overgrows early corroded pyrite grains.

#### Chert-Sulfide Breccia (Type 4)

One piece of chert-sulfide breccia (Type 4) was recovered in Core 158-957A-3X. It is comprised of clasts of red chert, red iron oxide, and porous massive pyrite and a matrix of gray to red chert (Fig. 7). Red chert also occurs as clasts within porous massive pyrite.

#### Massive Sulfide (Type 5)

The most abundant type of material recovered from Hole 957A is porous massive pyrite (Type 5a). These samples consist of granular to colloform pyrite, and are present in two of the three cores that recovered core (Cores 158-957A-1X and 3X). Some of these samples exhibit centimeter-sized clasts of chert and/or Fe-oxide (Fig. 8). In

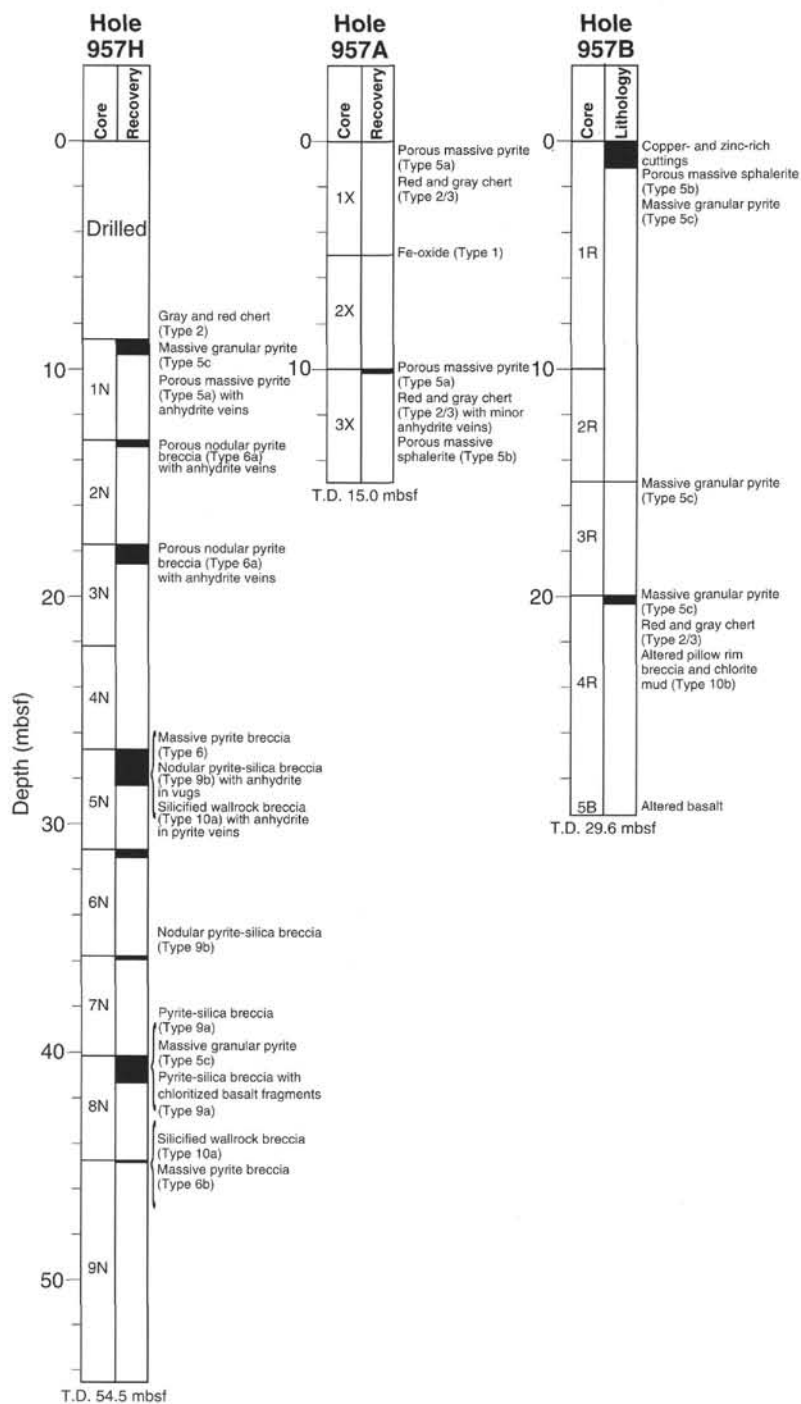


Figure 2. Schematic stratigraphic section of Holes 957H, 957A, and 957B.

polished thin section, pyrite morphology ranges from spherulitic aggregates to euhedral crystals. Much of the pyrite appears to replace marcasite, relics of which are common (Fig. 9). Marcasite, sphalerite, and a trace of chalcocopyrite are late minerals lining vugs. Sphalerite is mostly dark colored, as observed in hand specimen, but minor light-colored sphalerite is also present. One porous massive pyrite sample contains significantly more chalcocopyrite (up to 10 vol%).

Several small pieces of porous massive sphalerite (Type 5b), were also recovered in Core 158-957A-3X. The porous (>50%) massive

sphalerite pieces are similar in texture to white smoker samples present on the surface of the mound at the Kremlin area.

### Hole 957B

The top of the first core from Hole 957B (Core 158-957B-1R, from 0 to 9.9 mbsf) consists of 1 m of fine to coarse drill cuttings. Pieces of porous massive sphalerite and massive granular pyrite were also recovered. The second core had no recovery, and only one piece

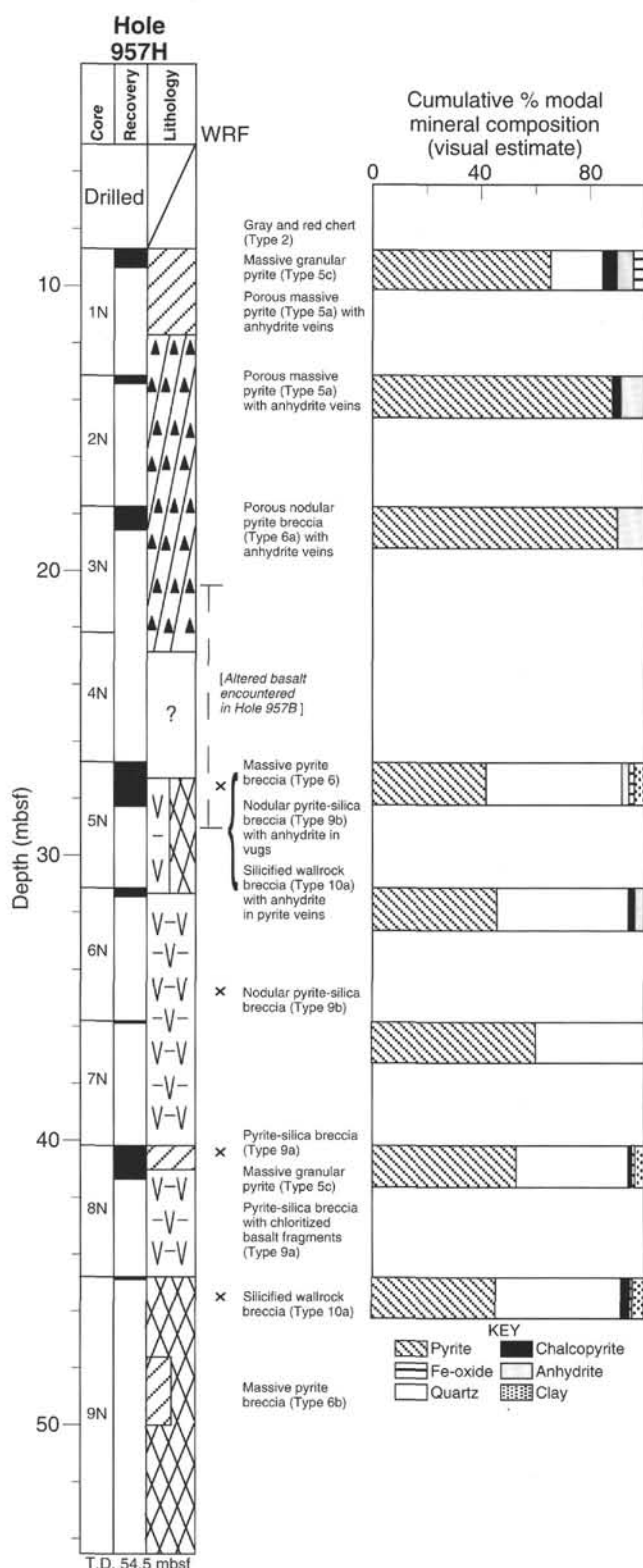


Figure 3. Schematic stratigraphic section of Hole 957H. The presence of wallrock fragments (WRF) is indicated by a small x. T.D. = total depth.

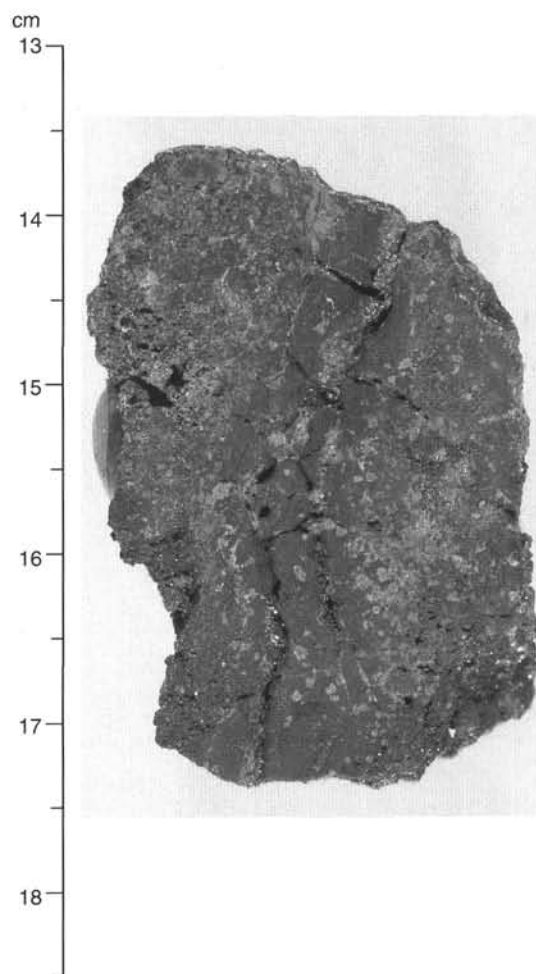


Figure 4. Photograph of Sample 158-957A-3X-1 (Piece 3, 13–18.5 cm), red chert, Type 2. The bulk of the sample consists of chalcedony stained red by iron oxide, with medium to coarse disseminated pyrite and chalcopyrite. The side and underside of the sample is coated with a mixture of sphalerite, pyrite, and anhydrite, which may be fracture fill. Fractures in the chert are variably filled with colorless silica, pyrite, and minor euhedral quartz and anhydrite.

of massive granular pyrite was recovered in the third core (Core 158-957B-3R, 14.9–19.9 mbsf). Core 158-957B-4R, from 19.9 to 29.6 mbsf, recovered a small (centimeter size) piece of massive pyrite, and a 3-cm-sized piece of red and gray chert, in addition to chloritic muds and basalt showing various degrees of alteration (see “Hydrothermal Alteration” section, this chapter).

#### Drill Cuttings

A 1.7-m interval of fine- to coarse-grained drill cuttings, composed of a mixture of Fe-oxide, red and gray chert, and pyrite grains and clasts was recovered from the upper part (0–9.9 mbsf) of Hole 957B. Bulk geochemical analysis of different size fractions was made (see “Sulfide Geochemistry,” this section).

#### Red and Gray Chert (Type 2)

A single sample of gray and red chert (Type 2; Sample 158-957B-4R-1, Piece 5) came from Core 158-957B-4R within the interval of altered basalt and chloritic mud (Fig. 10). The piece is composed of

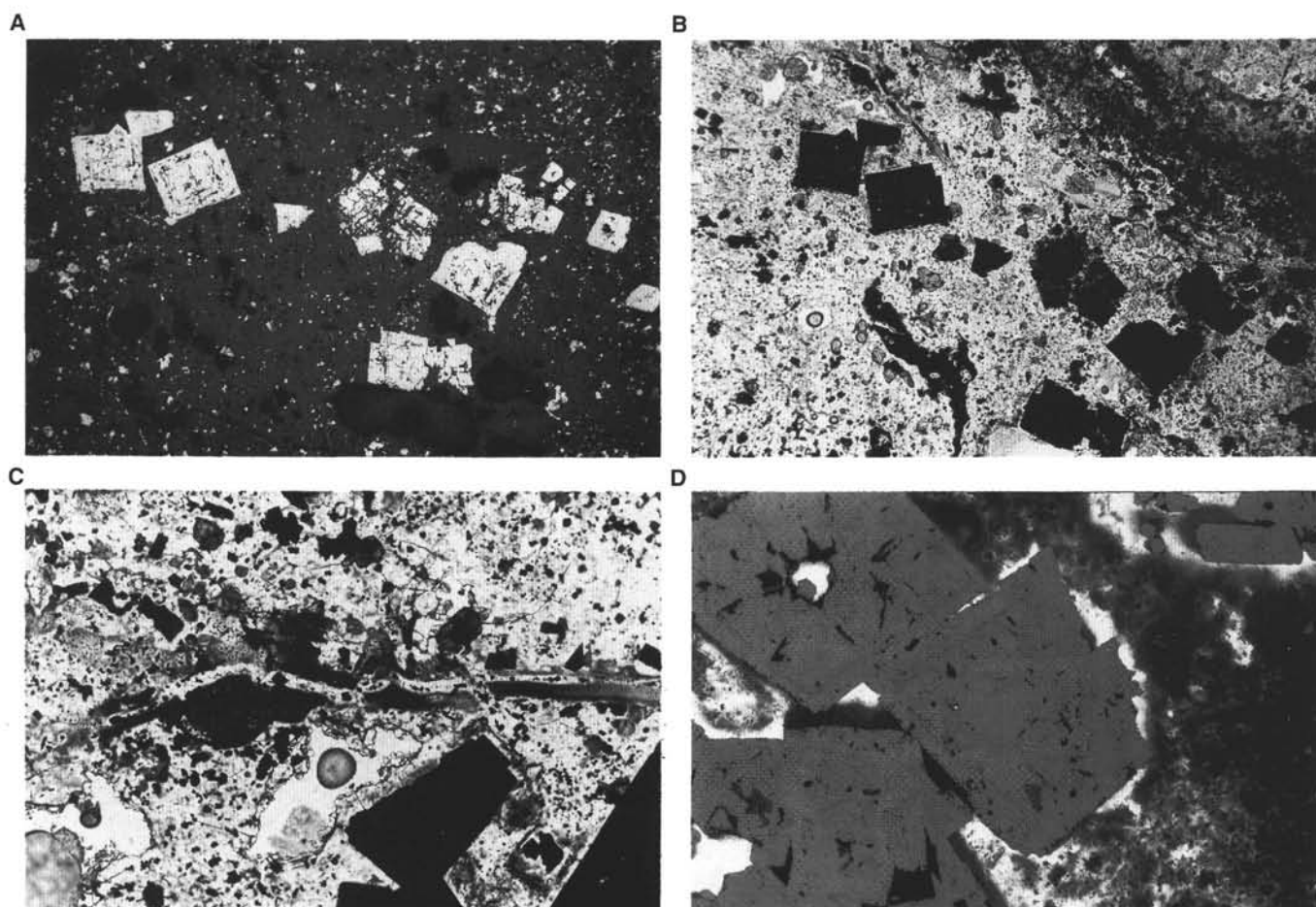


Figure 5. Photomicrographs of Sample 158-957A-3X-1 (Piece 9, thin section from 42 to 46 cm), red chert, Type 2. **A.** Euhedral pyrite grains (white) with some sphalerite (light gray), fractured and partially replaced by chalcedony (dark gray). Reflected light, field of view = 6 mm. **B.** The same field of view as in Figure 5A, but in transmitted light. **C.** Late quartz vein with pyrite (black) at its center, crosscutting Fe-oxide (dusty dark gray) and chalcedony (white); opaque grains are pyrite. Transmitted light, field of view = 1.5 mm. **D.** Euhedral pyrite (light gray) with corroded edges in chalcedony (white) and iron oxide (dark gray). Combined transmitted and reflected light, field of view = 1.5 mm.



Figure 6. Transmitted light photomicrograph of gray silica in Sample 158-957A-3X-1 (Piece 8, thin section from 38 to 42 cm), showing filamentous amorphous silica (white) with minor sulfides (black). Field of view = 750  $\mu\text{m}$ .

chalcedony with patches of quartz. The sample is mottled red by Fe-oxides, and minor disseminated pyrite is present. Small, irregular clasts of ocherous Fe-oxide material and gray green altered glass (now phyllosilicate) are enclosed in the silica (Fig. 11); Fe-oxide and phyllosilicate aggregates in the silica are also visible in thin section. The presence of altered glass implies that the stratigraphic position of this chert sample, within a sequence of altered basalt and chloritic mud, is correct, and that these silica-oxides formed as interpillow hydrothermal precipitates (see below).

#### *Massive Sulfide (Type 5)*

A single, 4-cm piece of massive sphalerite (Type 5b; Sample 158-957B-1R-2, Piece 2) was recovered in Core 158-957B-1R (Fig. 12). The sample is similar to pieces recovered between 10 and 15 mbsf in Hole 957A, and to white smoker material present on the surface of the mound. In polished thin section, multiple generations of sphalerite (translucent and yellow in transmitted light) and amorphous silica overgrow a framework of sphalerite, pyrite, and chalcocopyrite to form a porous structure (Fig. 13). This matrix encloses a small clast of amorphous silica stained red by disseminated Fe-oxides (Fig. 14).

A 7-cm piece of coarse-grained massive granular pyrite (Type 5c; Sample 158-957B-1R-2, Piece 3) was recovered in the interval from

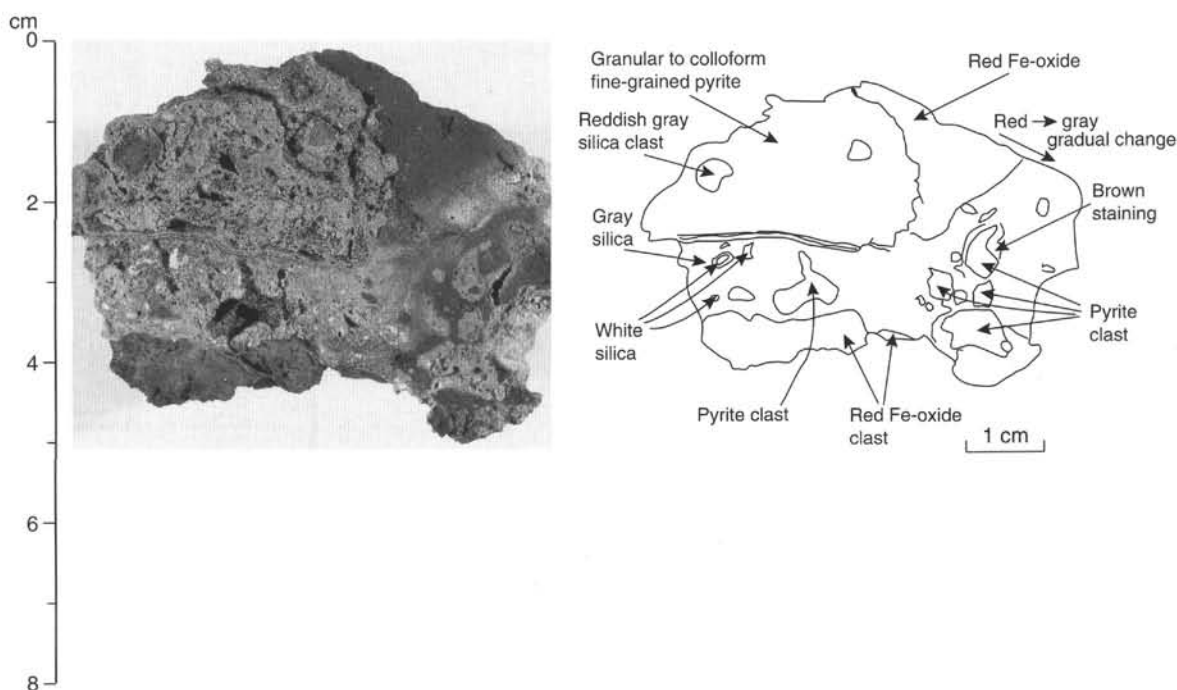


Figure 7. Photograph and descriptive sketch of Sample 158-957A-3X-1 (Piece 1, 0–8 cm), chert-sulfide breccia, Type 4.

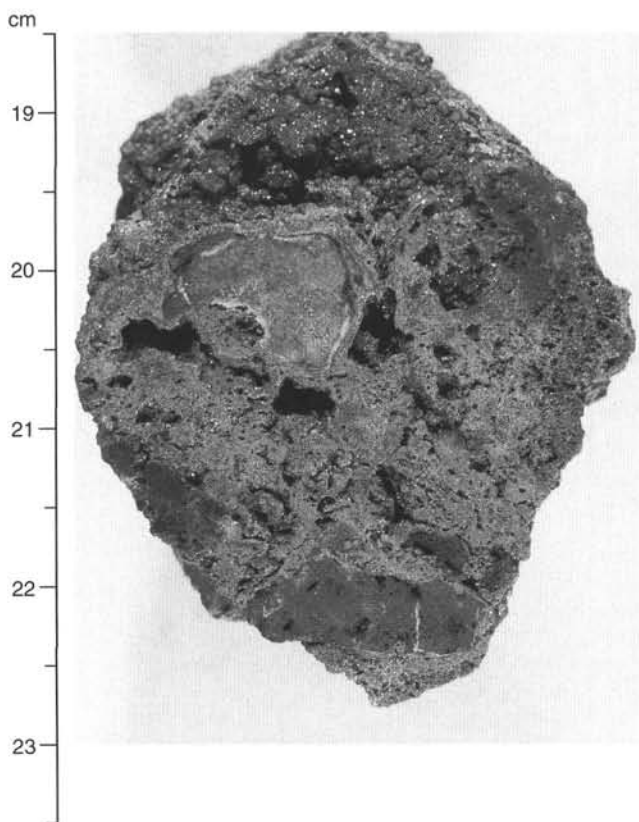


Figure 8. Photograph of Sample 158-957A-3X-1 (Piece 4, 18.5–23.5 cm), a piece of porous massive pyrite (Type 5a) containing subrounded to angular clasts of chert and Fe-oxide.

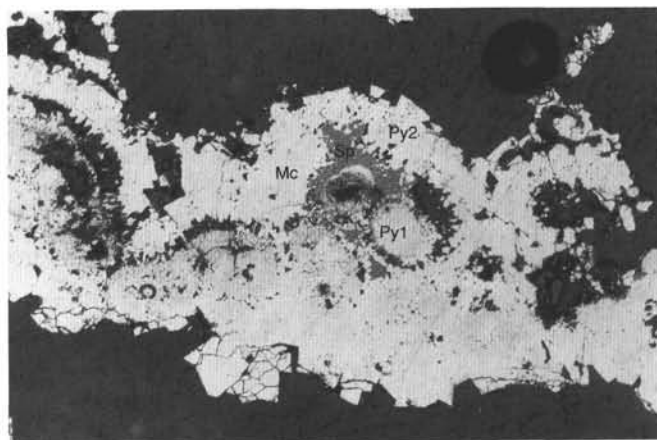


Figure 9. Reflected light photomicrograph of Sample 158-957A-3X-1 (Piece 11, thin section from 50 to 57 cm), porous massive pyrite, Type 5a, showing spheroidal pyrite (Py1) overgrown by sphalerite (Sp) and marcasite (Mc), and then by euhedral pyrite (Py2). Field of view = 750  $\mu\text{m}$ . Dark gray is epoxy.

0 to 9.9 mbsf. Another similar piece was recovered between 14.9 and 19.9 mbsf (Fig. 15). The pyrite mineralization differs from that seen in Hole 957A in that it is coarse grained, with a low porosity; it contains a trace amount of silica; and the proportions of chalcopryrite and sphalerite are significantly lower. In polished thin section, the absence of marcasite, the lack of primary growth textures (e.g., colloform growth), and the scarcity of other sulfides are indicative of recrystallization (Fig. 16). A small (1 cm) fragment of similar material (Sample 158-957B-4R-1, Piece 4) was recovered in the lower part of the final core (19.9–29.9 mbsf). These massive granular pyrite samples are generally coarser grained and contain less quartz and chalcopryrite than those in cores from Holes 957C and 957E (TAG-1 area).

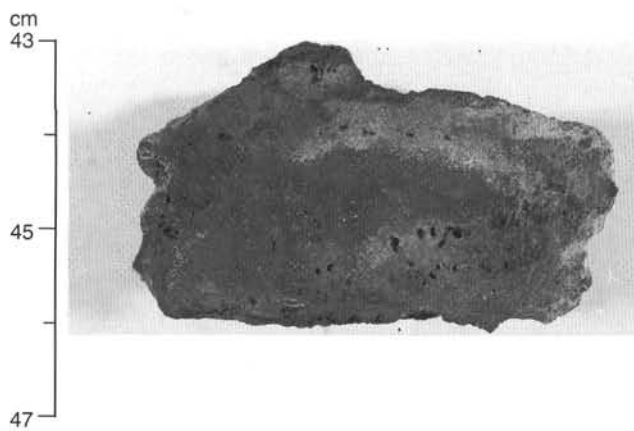


Figure 10. Red and gray chert in Sample 158-957B-4R-1 (Piece 5, 43–47 cm) with ocherous Fe-oxide and altered basalt glass fragments.

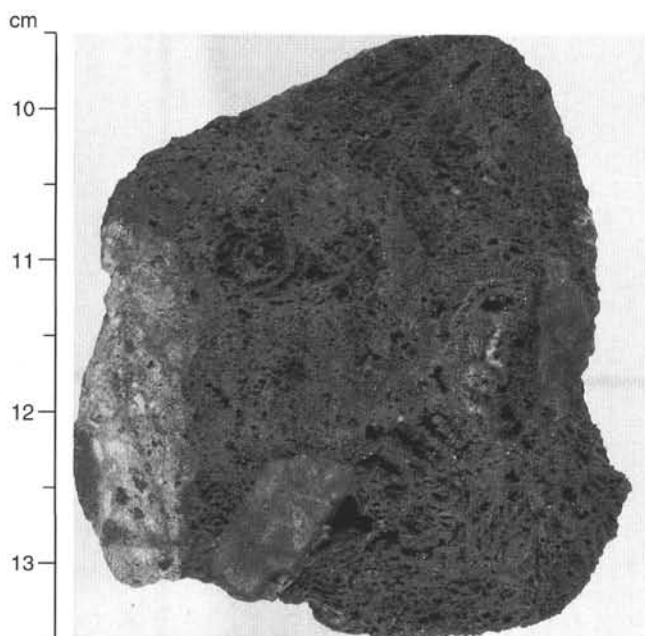


Figure 12. Porous massive sphalerite in Sample 158-957B-1R-2 (Piece 2, 9.5–13.5 cm), with a zone of light-colored amorphous silica. The porous sulfide structure encloses a small clast of red and gray amorphous silica.

### Altered Basalt

Core 158-957B-4R (19.5–29.5 mbsf) intersected altered pillow-rim breccia fragments enclosed in red and green chloritic mud and basalt (see “Hydrothermal Alteration” and “Igneous Petrology and Geochemistry” sections, this chapter).

### Hole 957H

Nine cores were recovered from Hole 957H. Gray and red cherts were recovered in the shallowest core (Section 158-957H-1N-1, 8.7–13.2 mbsf), but porous massive pyrites and porous nodular pyrite breccias are the dominant rock types above a depth of 27 mbsf (Sections 158-957H-1N-1 to 3N-1). Between 27 and 54.5 mbsf (Cores 158-957H-5N to 9X), nodular pyrite-silica breccias and silicified

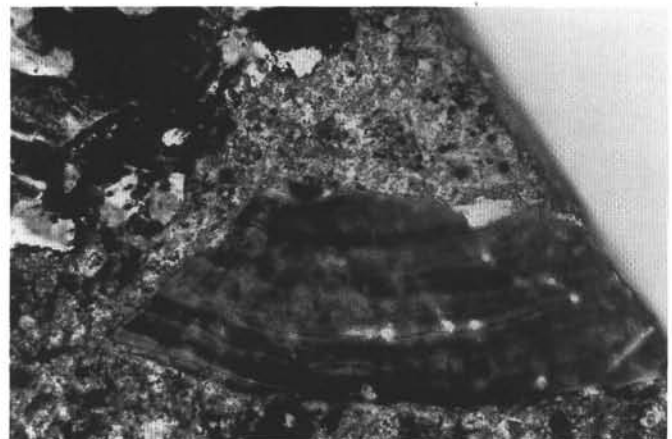


Figure 11. Transmitted light photomicrograph of an angular, banded glass fragment (now altered to fine clays, stained by iron oxide) in a matrix of chalcedony and quartz with disseminated Fe-oxide (dark gray and black), clay mineral aggregates (light to dark gray), and pyrite (black). Field of view = 1.5 mm. Sample 158-957B-4R-1 (Piece 5, thin section from 44 to 47 cm).

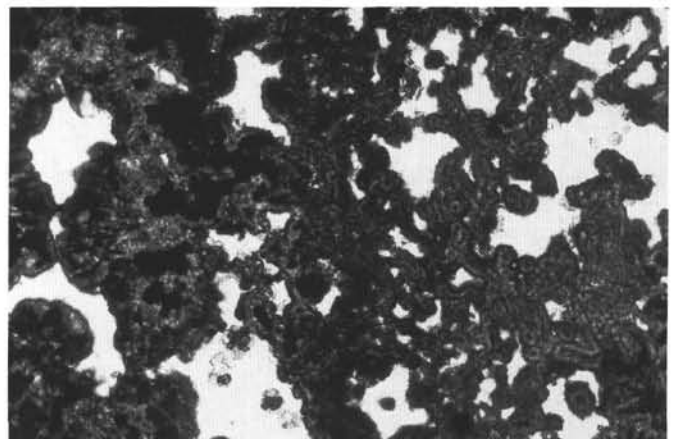


Figure 13. Transmitted light photomicrograph of massive sphalerite (shades of gray) forming distinctive porous aggregates. A later generation of coarse euhedral sphalerite (left of field) overgrows spheroidal pyrite and chalcopyrite (black) and lines a small conduit structure. Pore spaces are lined by a thin (<20  $\mu\text{m}$ ) layer of amorphous silica (translucent layer around white voids). Field of view = 1.5 mm. Sample 158-957B-1R-2 (Piece 2, thin section from 10 to 12 cm).

wallrock breccias, containing a few chloritized basalt fragments, are the dominant rock types recovered, with minor amounts of massive pyrite. Chalcopyrite is concentrated ( $\leq 5$  vol%) in the upper sections (Cores 158-957H-1N to 3N), but it occurs in only trace amounts in the deeper sections (Cores 158-957H-4N to 9X). Anhydrite, commonly as very coarse-grained euhedral crystals, occurs throughout the section as thin veins and filling vugs. Thick massive anhydrite veins, similar to those recovered from Hole 957C, were not recovered from Hole 957H.

### Gray and Red Chert (Type 2)

Three small pieces of chert (Type 2/3; one gray and two red), similar to samples recovered in Holes 957A and 957B, were recovered in Core 158-957H-1N. These samples are composed of silica, some stained red by very fine-grained iron oxide, with disseminated euhedral

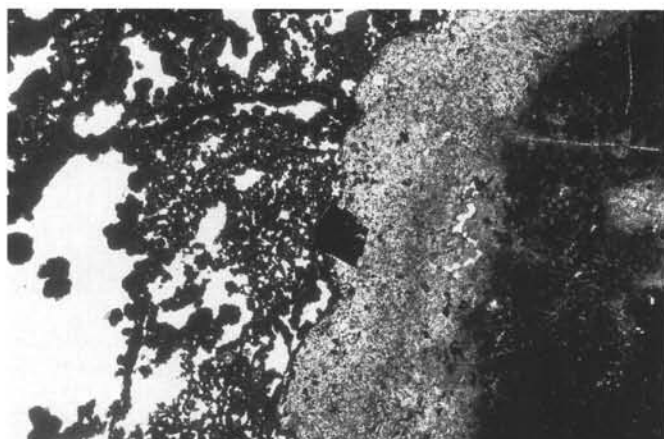


Figure 14. Transmitted light photomicrograph of an amorphous silica clast (with disseminated Fe-oxides, appearing dark gray or black), enclosed in a matrix of porous massive sphalerite (black to dark gray). White areas are pore spaces. Note the single, large, euhedral pyrite crystal (center), corroded along its contact with the silica. Field of view = 6 mm. Sample 158-957B-1R-2 (Piece 2, thin section from 10 to 12 cm).

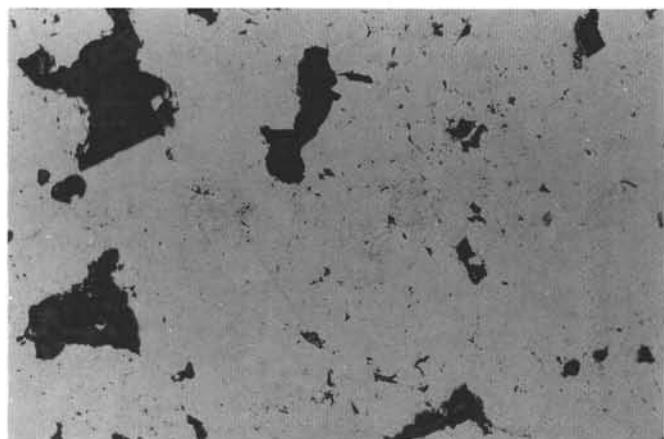


Figure 16. Reflected light photomicrograph of coarse-grained massive pyrite, with dusty, microporous traces of a primary colloform texture. Irregular inclusions of chalcopyrite ( $< 30 \mu\text{m}$ ) are present (darker gray in porous pyrite regions). Void space appears dark gray or black. Contrast this texture with the porous massive pyrite in Figure 9. Field of view = 1.5 mm. Sample 158-957B-3R-1 (Piece 1, thin section from 3 to 6 cm).

dral grains and small ( $< 1 \text{ mm}$ ) aggregates of pyrite and chalcopyrite. Pyrite, chalcopyrite, and very fine-grained euhedral quartz are present in vugs. Porosity is low (5% by visual estimate). Fine-grained euhedral anhydrite grains are present on outer surfaces, and in thin ( $< 1 \text{ mm}$  wide) veins.

#### **Massive Sulfide (Type 5)**

Porous massive pyrite (Type 5a) dominates the material recovered from above 13.2 mbsf (in Core 158-957H-1N), but it is not present in any other cores from Hole 957H. Samples exhibit primary colloform and dendritic textures and consist of very fine- to fine-grained euhedral and colloform pyrite, with minor amounts of fine-grained chalcopyrite and anhydrite. Porosity is high (21.5%; see "Physical Properties" section, this chapter). Fine- to medium-grained euhedral anhydrite is present filling vugs and as 1- to 5-mm-wide

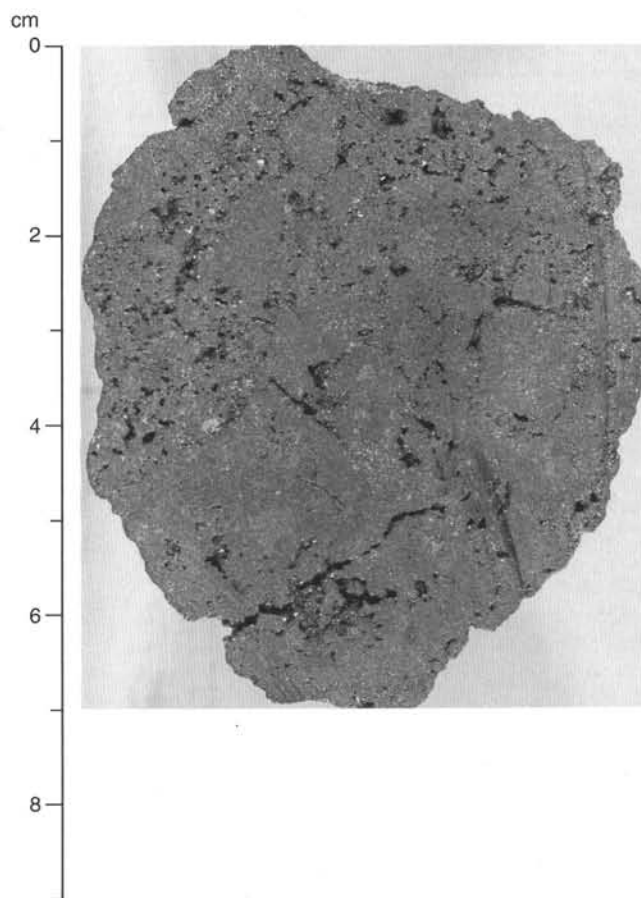


Figure 15. Massive pyrite, showing the lower porosity and coarser grain size than samples recovered from Hole 957A (e.g., see Fig. 8). These features are indicative of recrystallization. Sample 158-957B-3R-1 (Piece 1, 0-9 cm).

veins (Fig. 17). A single sample (Sample 158-957H-1N-1, Piece 9) is composed of porous massive pyrite, although it displays a distinctly clastic texture. Clasts are of fine-grained pyrite and chalcopyrite enclosed in colloform pyrite and anhydrite, and cut by thin anhydrite veins (Fig. 18). Except for the presence of anhydrite, the porous massive pyrite samples are similar in texture to chalcopyrite-rich porous massive pyrite recovered in Core 158-957A-1X from depths above 5 mbsf.

Massive granular pyrite (Type 5c) was also recovered in Core 158-957H-1N and in Cores 158-957H-5N and 8N. In Core 158-957H-1N, samples are composed of very fine- to fine-grained pyrite. In thin section, the majority of pyrite is present as  $500 \mu\text{m}$  anhedral to euhedral grains. Relict textures of colloform pyrite contain small ( $10 \mu\text{m}$ ) anhedral inclusions of chalcopyrite. Rare small ( $5 \mu\text{m}$ ) anhedral sphalerite inclusions were observed and trace amounts of chalcodony fill preexisting pore spaces. Minor amounts of anhydrite occur, along with chalcopyrite, on the outer surfaces of the samples. These samples are similar to, but finer grained than, massive granular pyrite recovered from Hole 957B. Massive granular pyrite recovered from greater depths (Samples 158-957H-5N-1, Piece 1, and 8N-1, Piece 10) exhibit lower porosity (by visual estimate) and more interstitial quartz.

#### **Massive Pyrite Breccias (Type 6)**

A single sample of massive pyrite breccia that exhibits complex textures, including angular clasts of massive granular pyrite and

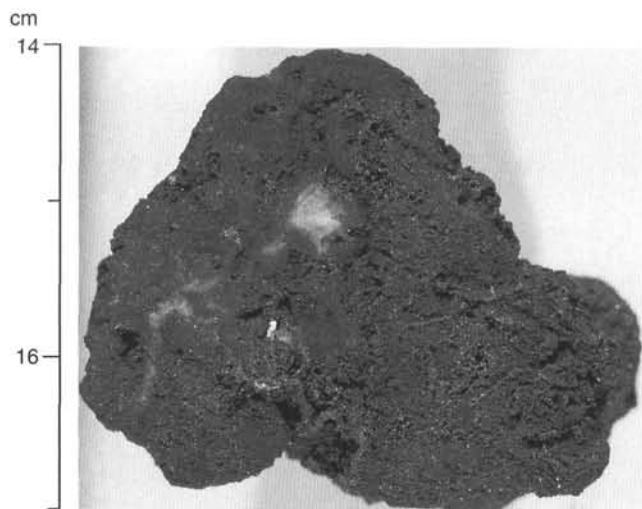


Figure 17. Sample 158-957H-1N-1 (Piece 5, 14–17 cm), Type 5a, composed of fine-grained pyrite, exhibiting primary depositional textures, with minor amounts of chalcopyrite, as well as anhydrite filling vugs and as veins.

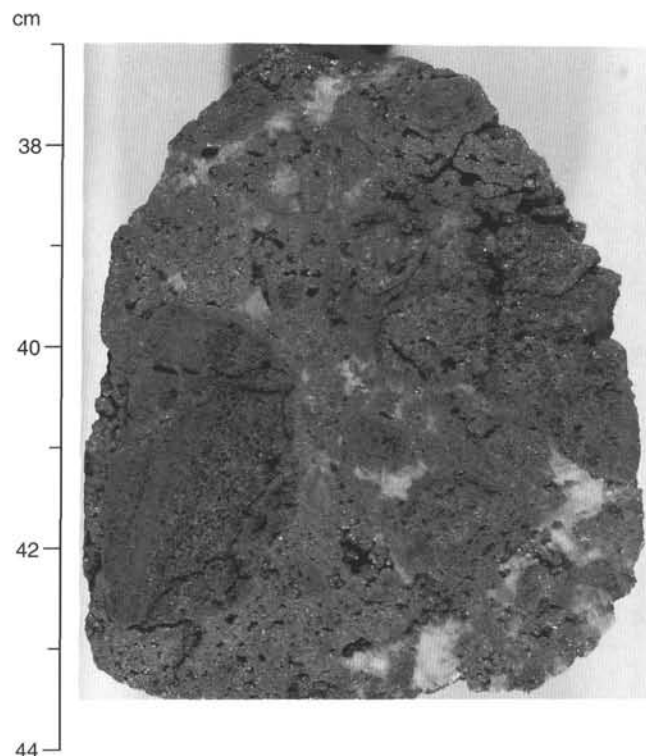


Figure 18. Sample 158-957H-1N-1 (Piece 9, 37–44 cm), Type 5a, which consists of clasts of porous massive pyrite enclosed in colloform pyrite and anhydrite, cut by thin anhydrite veins.

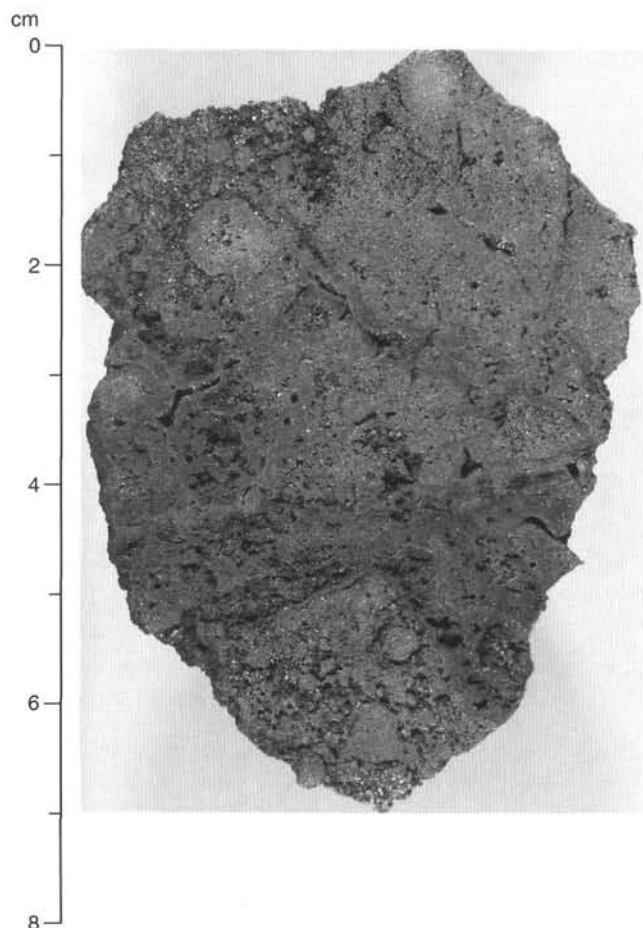


Figure 19. Massive pyrite breccia (Sample 158-957H-3N-1, Piece 1, 0–8 cm), Type 6, with angular clasts of massive granular pyrite overgrown and cemented by bands of colloform pyrite and marcasite.

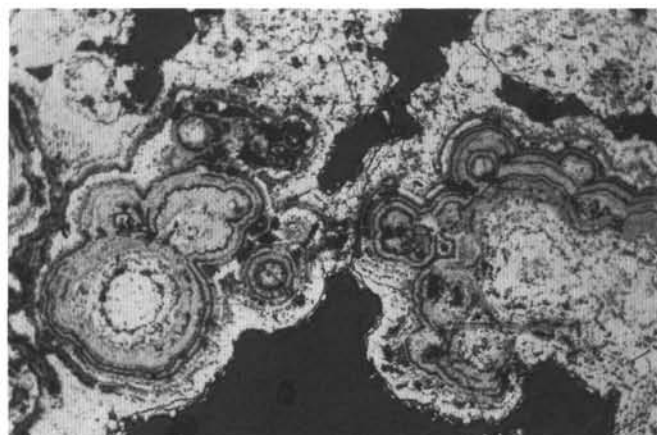


Figure 20. Colloform pyrite (medium gray) associated with polycrystalline pyrite-marcasite (white). Dark gray is epoxy. Reflected field of view = 1.5 mm. Sample 158-957H-3N-1 (Piece 1, thin section from 5 to 7 cm).

bands of colloform marcasite, was recovered in Core 158-957H-3N in the interval from 17.7 to 22.2 mbsf (Fig. 19). Clasts are overgrown and cemented by porous, colloform-banded, polycrystalline pyrite and marcasite. In thin section, pyrite morphology ranges from euhedral to colloform (Fig. 20). Angular clasts consist of aggregates of anhedral to euhedral pyrite with trace amounts of chalcopyrite and sphalerite as inclusions, and with late marcasite filling spaces. Sphalerite also occurs as late crystals, with chalcopyrite and marcasite rimming the pyrite. Light-colored translucent sphalerite is

present as euhedral crystals up to 40  $\mu\text{m}$ , and as bands alternating with marcasite. Trace amounts of amorphous silica partially fill voids between pyrite/marcasite aggregates. Void space is high (25 vol%), as estimated from thin-section observations.

Porous nodular pyrite breccias (Type 6a) were recovered in the first three cores of Hole 957H, from 8.7 to 22.2 mbsf. Samples consist of 80% to 95% very fine- to medium-grained pyrite as massive nodular aggregates (0.1 to >5 cm) and as individual grains in the pyrite-anhydrite matrix. Trace to minor amounts of fine-grained chalcopryrite occur in the matrix, in veins, and as nodular clasts. Minor amounts of fine- to coarse-grained anhydrite (as large as 3 mm) are present in 0.5- to 5-mm-wide veins and as matrix (Figs. 21, 22A). Pyrite nodules consist of euhedral grains, forming polycrystalline aggregates with abundant chalcopryrite. Pyrite at the core of the aggregates contains 2- to 5- $\mu\text{m}$  anhedral inclusions of sphalerite and hematite (Fig. 22B). Hematite was not observed in porous nodular pyrite breccias from Holes 957C or 957E. A later generation of euhedral pyrite, partially replaced by chalcopryrite, forms an outer rim on the aggregates (Fig. 22C). Other than the presence of hematite, these samples are similar to the porous nodular pyrite breccias and massive pyrite-anhydrite breccias recovered in Hole 957C (TAG-1 area).

Two pieces of massive pyrite breccia (Type 6b) were recovered in Core 158-957H-9X, from a depth interval of 44.7 to 54.5 mbsf. These pieces are composed dominantly of grains and aggregates of euhedral pyrite, with chalcopryrite and anhydrite present on broken surfaces. As much as 16 vol% quartz is present in the breccia matrix and lining vugs. The outer margins of samples are composed of mixed pyrite,

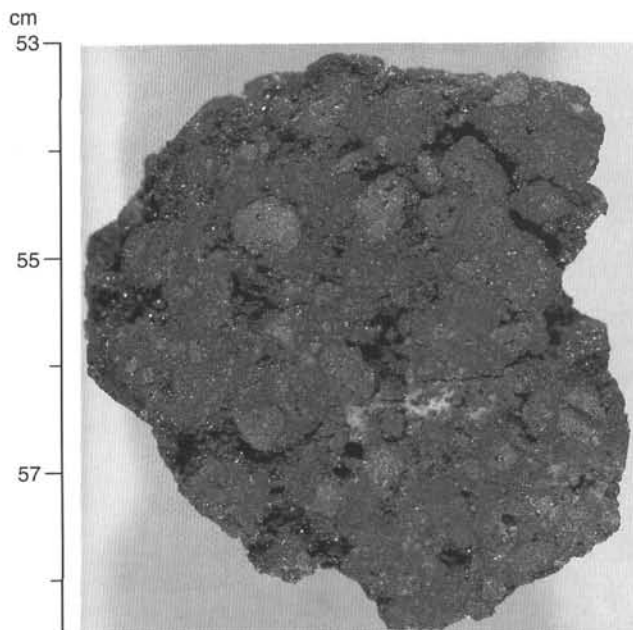


Figure 21. Porous nodular pyrite breccia (Type 6a) composed of nodular aggregates of pyrite in a matrix of pyrite and anhydrite (Sample 158-957H-1N-1, Piece 12, 53–58 cm). Anhydrite is present in thin veins and in vugs.

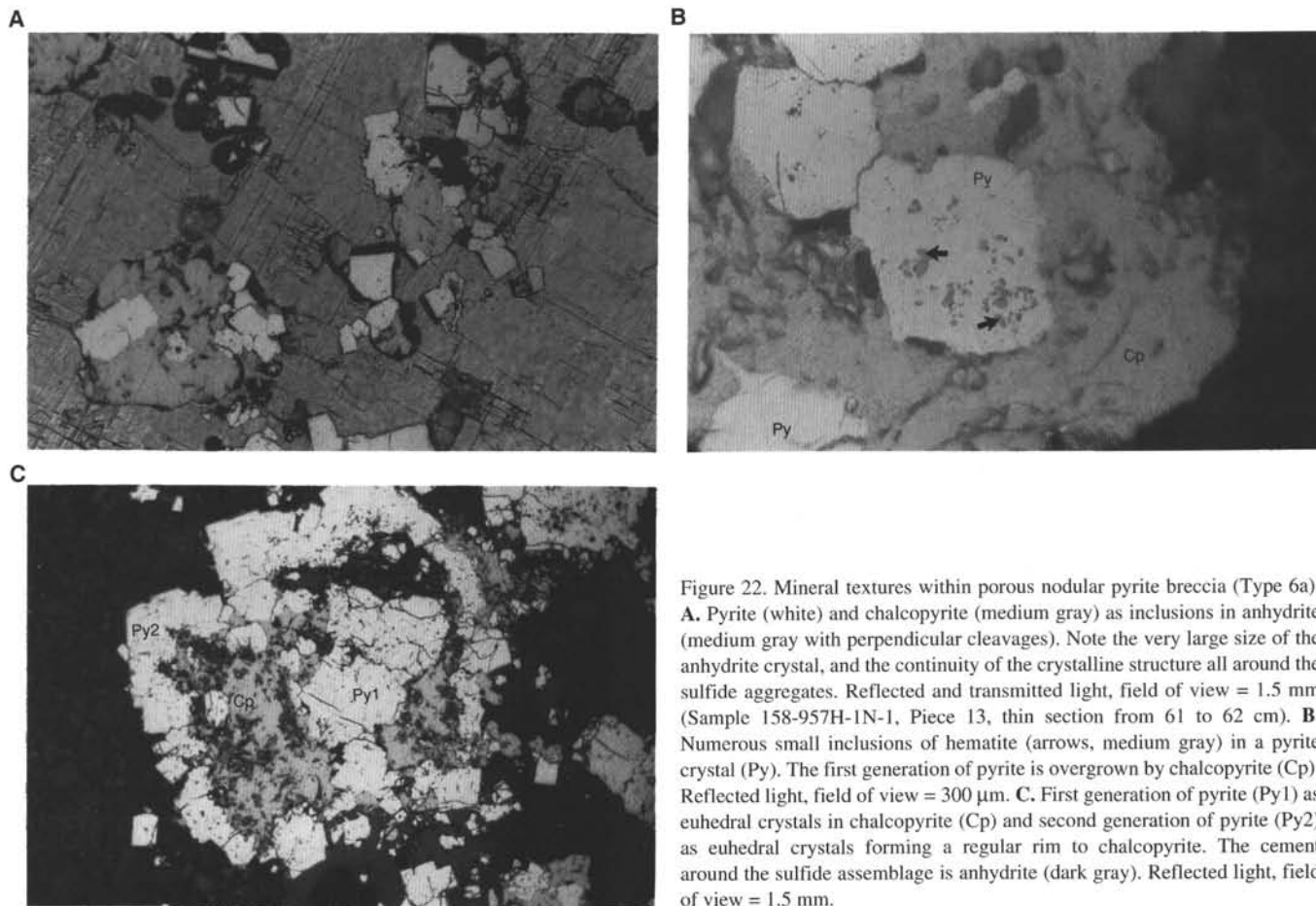


Figure 22. Mineral textures within porous nodular pyrite breccia (Type 6a). **A.** Pyrite (white) and chalcopryrite (medium gray) as inclusions in anhydrite (medium gray with perpendicular cleavages). Note the very large size of the anhydrite crystal, and the continuity of the crystalline structure all around the sulfide aggregates. Reflected and transmitted light, field of view = 1.5 mm (Sample 158-957H-1N-1, Piece 13, thin section from 61 to 62 cm). **B.** Numerous small inclusions of hematite (arrows, medium gray) in a pyrite crystal (Py). The first generation of pyrite is overgrown by chalcopryrite (Cp). Reflected light, field of view = 300  $\mu\text{m}$ . **C.** First generation of pyrite (Py1) as euhedral crystals in chalcopryrite (Cp) and second generation of pyrite (Py2) as euhedral crystals forming a regular rim to chalcopryrite. The cement around the sulfide assemblage is anhydrite (dark gray). Reflected light, field of view = 1.5 mm.

chalcopyrite, and quartz, and are similar to veins observed in samples from Holes 957C and 957E. These samples may represent pieces of vein or vein selvage.

### **Pyrite-Silica Breccia (Type 9)**

Pyrite-silica breccias (Type 9a) were recovered in Core 158-957H-8N in the interval from 40.2 to 44.7 mbsf. These matrix-supported breccias consist of 50 to 70 vol% pyrite as fine- to coarse-grained disseminations, aggregates, and clasts (up to 2.5 cm) set in a matrix of very fine- to fine-grained, gray to white quartz (Fig. 23). Minor amounts of chalcopyrite are present as fine-grained discrete aggregates and within pyrite clasts. Clasts of red and gray silica, silicified altered basalt, and silicified hyaloclastite are also present. Trace amounts of fine- to medium-grained fibrous anhydrite are present on the outer surfaces of samples. Botryoidal quartz lines vugs. In some samples, very fine-grained, green phyllosilicate (chlorite?) is dispersed throughout the matrix and associated with pyrite. Some altered basalt clasts are cut by pyrite veins similar to Stage 2 veining (see "Sulfide Petrology and Geochemistry" section, Chapter 7, this volume) in samples recovered from Hole 957E (Samples 158-957H-8N-1, Pieces 8 and 11). Very fine-grained, euhedral crystals of an unidentified mineral (translucent ruby red to violet; hematite?) overgrowing quartz and lining vugs were observed in several samples (Samples 158-957H-8N-1, Pieces 10, 12, and 13).

In thin section, 20- to 50- $\mu\text{m}$ , fibrous chalcedony grains enclose pyrite clasts. Fractures within recrystallized pyrite aggregates are filled by fibrous chalcedony, with some replacement of the pyrite (Fig. 24A). Chalcedony forms a low-porosity matrix between the pyrite aggregates (Fig. 24B). Composite pyrite-quartz clasts are com-

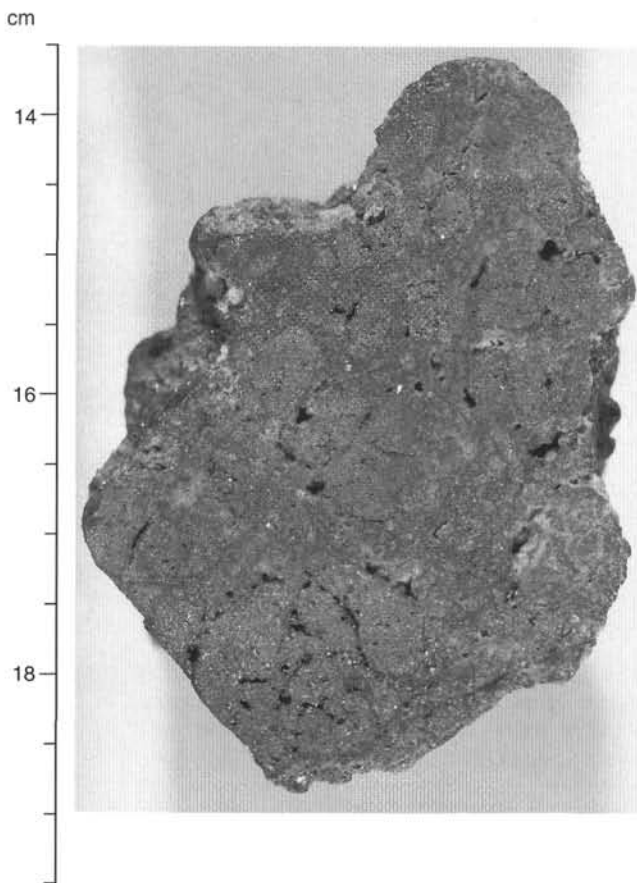


Figure 23. Pyrite-silica breccia (Type 9a) composed of grains, clasts, and aggregates of pyrite in a matrix of gray to white quartz (Sample 158-957H-8N-1, Piece 3, 13.5–19.5 cm).

monly rimmed by a second generation of pyrite. Minor chalcopyrite, associated with a trace of sphalerite, also occurs as fine (<50  $\mu\text{m}$ ) inclusions within pyrite grains. Rare, late anhydrite is dominantly associated with chalcopyrite and pyrite, and with hexagonal (20  $\mu\text{m}$ ), very thin plates of hematite that form clusters of crystals at the surface of chalcedony. These are probably the equivalent of the unidentified red crystals overgrowing quartz and lining vugs observed in hand sample (Samples 158-957H-8N-1, Pieces 10, 12, and 13). Except for the occurrence of the ruby red mineral and hyaloclastite, and a greater abundance of pyrite, these pyrite-silica breccias are similar to those recovered from Holes 957C and 957E (TAG-1 area).

Nodular pyrite-silica breccias (matrix-supported) (Type 9b) occur in the interval from 26.7 to 40.2 mbsf (Sections 158-957H-5N, 6N, and 7N). Very fine-grained, euhedral grains and 1- to 20-mm, rounded clasts of pyrite occur in a matrix of very fine-grained quartz (Fig. 25). Trace amounts of chalcopyrite occur in pores of some pyrite clasts, as 2- to 3-mm aggregates, and as 1-mm selvages on anhydrite veins. Very coarse-grained (as large as 6 mm) anhydrite lines large centimeter-sized vugs and is present in veins up to 1 cm wide (Fig. 25). Abundant rounded siliceous clasts (up to 5 cm), consisting of gray to white quartz plus variable amounts of pyrite and disseminated red Fe-oxide (hematite?) and, rarely, altered hyaloclastite, are also present. Angular fragments (<2 cm) of altered basalt (pale brown clay with disseminated pyrite) were observed in Samples 158-957C-6N-1, Pieces 1 and 2 (see detailed discussion in "Hydrothermal Alteration" section, this chapter).

### **Silicified Wallrock Breccia (Type 10)**

Clast- and matrix-supported silicified wallrock breccias (Type 10a) were observed in two cores (Sections 158-957H-5N-2, 27.6–31.2 mbsf, and 9X-1, 44.7–54.5 mbsf) from Hole 957H. Clasts of silicified basalt, silicified altered hyaloclastite, red and gray silica, and massive pyrite are cemented by white to gray quartz (Fig. 26). The general clast components are similar to the pyrite-silica breccias described above, but silicified wallrock breccias are distinguished by a high proportion of recognizable altered basalt material. In Section 158-957H-5N-2, silicified clasts represent 70 vol% of the whole section. Red Fe-oxide (hematite?) and chlorite are disseminated throughout many of the silicified clasts. Pyrite occurs as disseminations in the silicified clasts, as 1- to 20-mm, rounded clasts, and as millimeter-thick rims around the silicified clasts. Up to 10% very fine-grained, pale brown clay is present within the silicified wallrock clasts (see "Hydrothermal Alteration" section, this chapter). Fine- to very coarse-grained anhydrite occurs in veins and lines vugs and pore space (Fig. 27). Pyrite and chalcopyrite occur with fine-grained anhydrite in the anhydrite veins.

In thin section (Sample 158-957H-5N-2, Piece 3A), the matrix of the breccias is a mixture of fine-grained pyrite and quartz. Anhedral pyrite, with abundant euhedral quartz inclusions, is corroded and replaced by quartz. Subhedral to euhedral pyrite contains few quartz inclusions. Quartz, in general, contains abundant submicron inclusions, which gives it a "dirty" appearance. Euhedral quartz has fewer inclusions and rare zonation. Late anhydrite occurs filling pore space in the massive pyrite, in late cracks, and rarely in interstices of the pyrite-quartz matrix. The altered basalt clasts are brecciated and partly replaced by a network of small quartz-pyrite veins. Rare relics of basaltic texture are present (see "Hydrothermal Alteration" section, this chapter). Pyrite dominates this vein assemblage and shows in places a porous core. Quartz forms an irregular outer rim (10–20  $\mu\text{m}$ ) around the pyrite and grows perpendicular to the basalt clast. Angular massive pyrite clasts have corroded boundaries at the contact with the matrix. Aggregates have indications of recrystallization (individual grains commonly >400  $\mu\text{m}$ ) and are overgrown by a thin layer of more porous pyrite (50–100  $\mu\text{m}$ ). The silica clasts are composed of quartz with abundant Fe-oxides and are fractured and infilled with quartz from the surrounding quartz-pyrite matrix. Clays are present

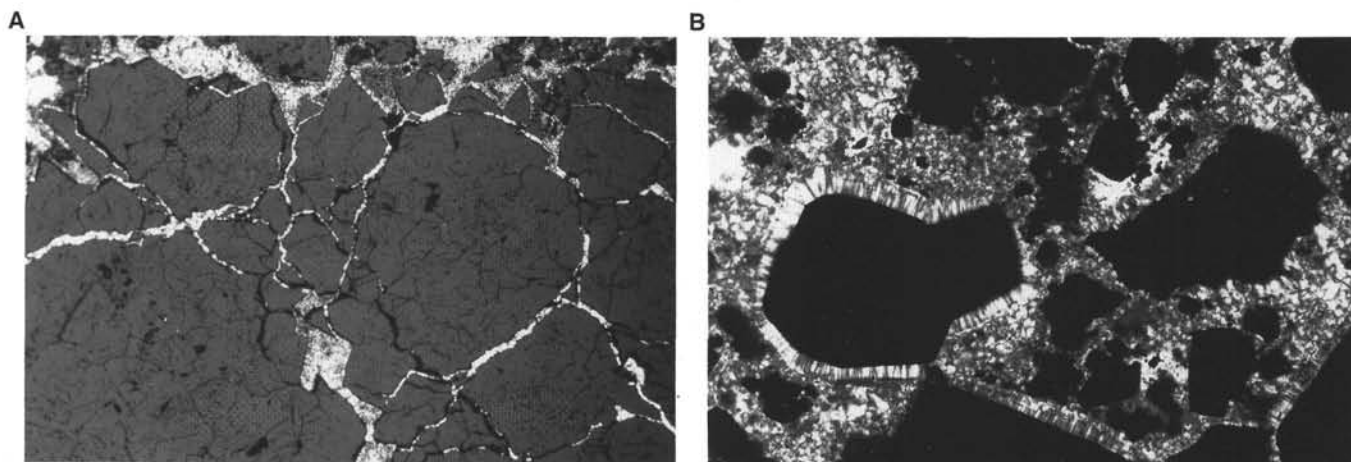


Figure 24. Mineral textures in the pyrite-silica breccia (Type 9a). **A.** Brecciated clast of recrystallized massive pyrite (gray) cemented by chalcedony (white). Reflected and transmitted light, field of view = 6 mm. **B.** Euhedral pyrite (black) in a matrix of chalcedony (gray and white) within pyrite-silica breccia (Type 9a). Note the regular rim of chalcedony fibers perpendicular to the surface of the pyrite crystals. Reflected light, field of view = 1.5 mm (Sample 158-957H-8N-1, Piece 14, thin section from 94 to 96 cm).

in the altered basalt but also in “dirty” quartz with iron oxides. Matrix and clasts are rimmed (in places clearly veined) by massive pyrite, which seems to be the same generation as pyrite in the basaltic clasts.

### Hole 957N

Hole 957N, located 5 m west of Hole 957A, was drilled to a depth of 40 m. Red and gray chert (Type 2), pyrite-silica-anhydrite breccia (Type 8), and nodular pyrite-silica breccia (Type 9b) were recovered in the single wash core (Core 158-957N-1W) from this 40 m interval (Table 2). All of these rock types except pyrite-silica-anhydrite breccias were recovered in Holes 957A, 957B, and 957H. The most similar samples from the TAG-2 area to the pyrite-silica-anhydrite breccias are porous nodular pyrite breccia samples in cores from Hole 957H that contain up to 15 vol% anhydrite as veins. These samples lie stratigraphically lower than chert and porous massive pyrite samples, and higher than nodular pyrite-silica breccias in core from Hole 957H. The pyrite-silica-anhydrite breccias from Hole 957N also lie stratigraphically lower than chert samples and higher than nodular pyrite-silica breccias.

#### Red and Gray Chert (Type 2)

A small piece of red chert, and a larger piece of dark gray chert, were recovered at the top of Core 158-957N-1W. These pieces consist of 10 vol% fine-grained pyrite disseminated in very fine-grained silica (Fig. 28). Light gray silica clasts, with fewer pyrite inclusions, are also present. Trace amounts of fine-grained, euhedral sphalerite occur on the surface of the gray chert sample. In thin section, cryptocrystalline aggregates of chalcedony and quartz dominate. A trace of amorphous silica is present as rounded aggregates enclosed in chalcedony. Sphalerite is present in trace amounts overgrowing pyrite and as inclusions in pyrite and chalcocopyrite. Chalcocopyrite, partly replaced by bornite, covellite, and digenite, overgrows and replaces pyrite, and is present interstitial to chalcedony. Except for the presence of bornite, covellite, and digenite, and of silica clasts, these samples resemble chert samples recovered in cores from Holes 957A, 957B, and 957H.

#### Pyrite-Silica-Anhydrite Breccia (Type 8)

Two pieces of matrix-supported pyrite-silica-anhydrite breccia, containing 70 vol% very fine-grained silica intermixed with minor anhydrite as matrix, and 20 vol% fine-grained pyrite as nodular clasts

and disseminated in the matrix, were recovered in Core 158-957N-1W (Fig. 29). Anhydrite is also present in narrow, irregular (1–2 mm) veins. Trace amounts of Fe-oxide occur in small siliceous clasts. Chalcocopyrite is present in trace amounts as very fine grains in pyrite + chalcocopyrite aggregates. In thin section, euhedral pyrite with inclusions of quartz, chalcocopyrite, and/or sphalerite occurs as grains and aggregates in a matrix of anhydrite and quartz. Anhydrite, present as polycrystalline aggregates, contains inclusions of euhedral quartz and appears to be late relative to quartz. Trace amounts of iron oxide in pyrite, and brown clay in quartz aggregates, are present. These samples are similar to pyrite-silica-anhydrite breccias recovered in cores from Hole 957C at the TAG-1 area. The only difference between the pyrite-silica-anhydrite breccias from Hole 957N and the porous nodular pyrite breccias with anhydrite veins from Hole 957H is the presence of anhydrite in the matrix of the former.

#### Nodular Pyrite-Silica Breccia (Type 9b)

Five pieces of nodular pyrite-silica breccias were recovered in the lower part of Core 158-957N-1W. These samples are similar to nodular pyrite-silica breccias from Hole 957H, and Holes 957C and 957E (TAG-1 area). The dark gray matrix is composed of very fine-grained silica with disseminated very fine-grained pyrite. Pyrite is also present as nodules and silica is also present as light gray clasts which contain trace amounts of Fe-oxide and chalcocopyrite. Anhydrite is present in minor amounts in 1- to 5-mm-wide veins.

### Sulfide Geochemistry

The chemical compositions of four samples from Holes 957B and 957H are presented in Table 4. Concentrations of Fe, Cu, Zn, Pb, Ag, Cd, and S were determined using the techniques outlined in the “Sulfide Petrology and Geochemistry” section of Chapter 5 (this volume). Two samples were analyzed for Au by ASV (see “Sulfide Petrology and Geochemistry” section, Chapter 7, this volume). Samples were selected from depths of 0 to 31.3 mbsf. These samples include drill cuttings from the top (0–1.03 mbsf) of Core 158-957B-1R-1, and three samples from Hole 957H recovered at depths of 9.30, 27.30, and 31.34 mbsf.

Metal concentrations of analyzed samples scatter over a wide range. The Fe contents of the samples range from 20.1 to 32.7 wt%. The range is slightly narrower than observed in the TAG-1 area, but the sample set is small and therefore less representative. Sulfur contents vary from 23.5 to 43.8 wt%.

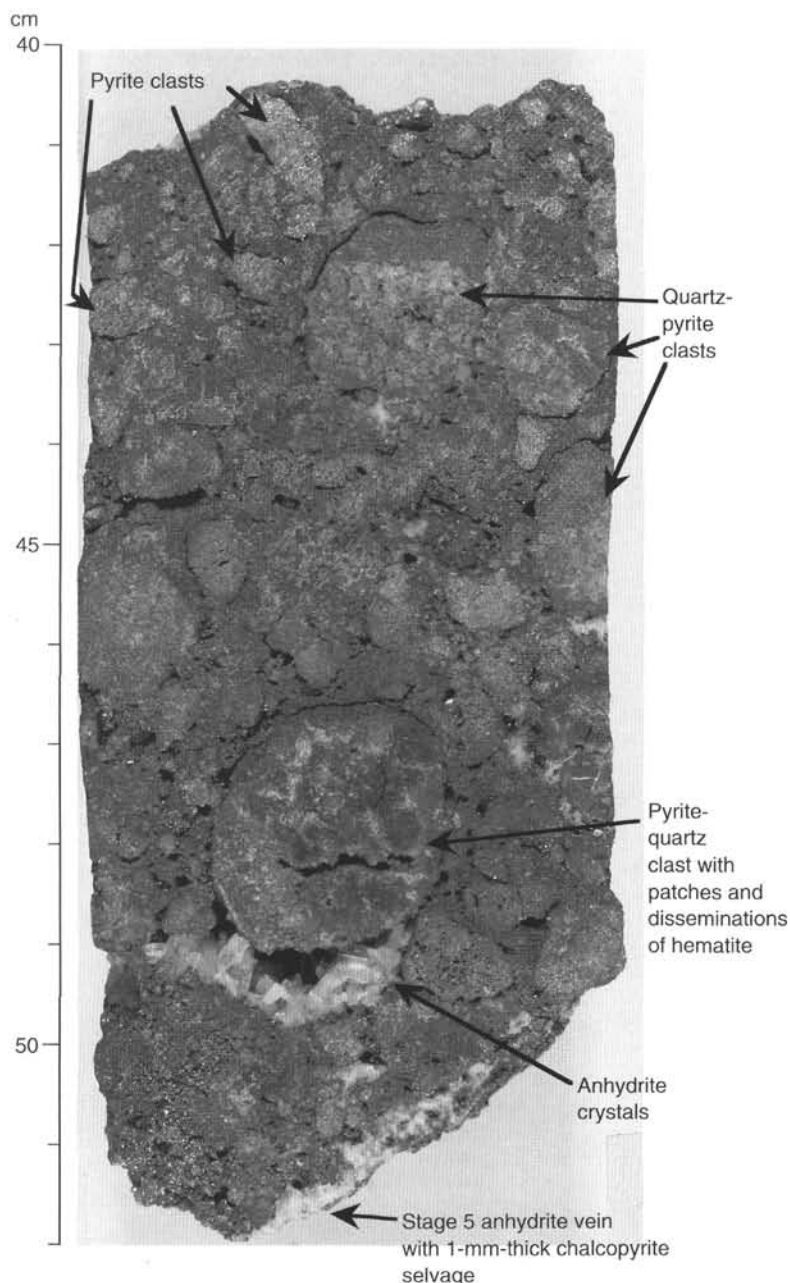


Figure 25. Nodular pyrite-silica breccia (Type 9b) with rounded clasts of pyrite and quartz with pyrite set in a matrix of quartz. Largest clast contains patches and disseminations of hematite. Coarse-grained anhydrite crystals line void space. Stage 5 anhydrite vein (see "Sulfide Petrology and Geochemistry" for TAG-1 area) with thin selvage of chalcopyrite cuts across breccia. Sample 158-957H-5N-1 (Piece 5B, 40–52 cm).

The most distinctive features of the samples in the TAG-2 area are the very high concentrations of Cu, Zn, Ag, Pb, and Cd in the sample near the surface (Sample 158-957B-1R-1, drill cuttings). Concentrations of Cu, Ag, and Pb found in this sample are the highest of all the samples analyzed. Metal concentrations in the deeper part of this area are low and within the range of those in the TAG-1 area.

#### **Chemical Composition of Different Rock Types**

The rock types analyzed on board include Fe-oxides (Type 1), porous, nodular pyrite breccia (Type 6a), and nodular pyrite-silica breccia (Type 9b).

#### **Fe-oxides (Type 1)**

Only one sample of this type was analyzed; it consists of drill cuttings recovered between 0.03 and 0.95 mbsf in Section 158-957B-1R-1. Before being analyzed, the cuttings were sieved into three fractions (>420, 63–420, and <63  $\mu\text{m}$ ) in an attempt to determine the chemical composition of the different grain sizes. All three fractions show very high concentrations of Cu, Zn, Ag, and Cd compared with samples from Hole 957H deeper within the section (Table 4). Concentrations of Fe, Cu, and Pb in the fine- and medium-sized (<63 and 63–420  $\mu\text{m}$ ) fraction are higher than those in the coarse (>420  $\mu\text{m}$ ) fraction, whereas concentrations of Zn, Ag, and Cd in the fine (<63  $\mu\text{m}$ ) fraction are lower than in the coarse and medium size (63–420

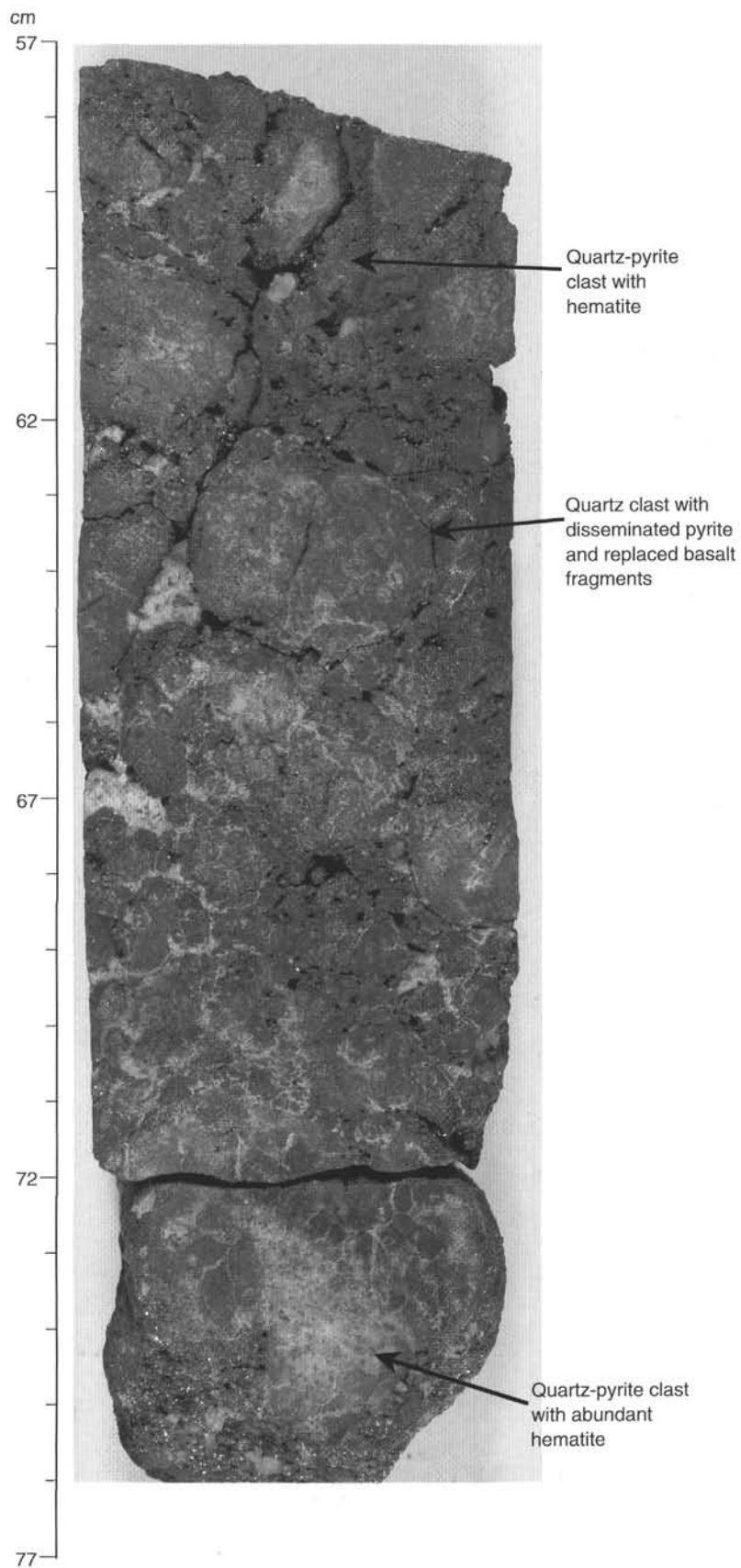


Figure 26. Silicified wallrock breccia (Type 10a) containing 1- to 3-cm basalt clasts in a matrix of gray quartz plus pyrite. Large (4 cm) siliceous clast of light gray quartz with disseminated pyrite and red iron oxide/oxyhydroxide stain also present at 72–76 cm. White veins are late anhydrite. Some quartz clasts contain abundant hematite (Sample 158-957H-5N-2, Pieces 3A–B, 57–77 cm).

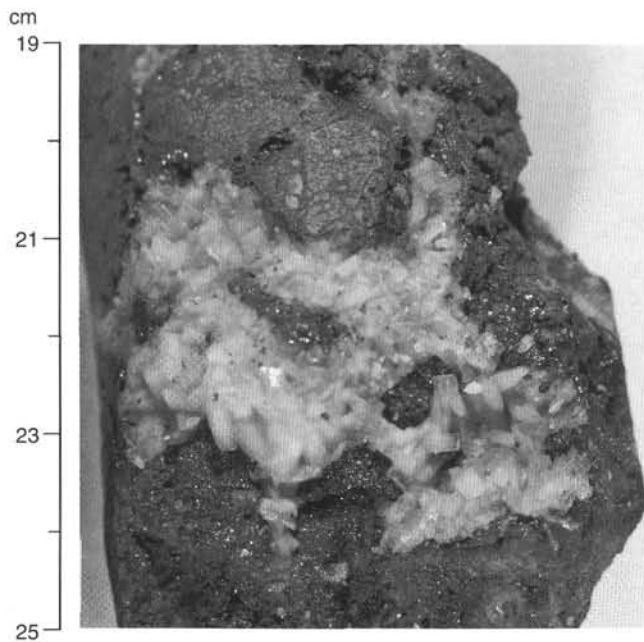


Figure 27. Coarse grains of anhydrite as veins and lining vugs in silicified wallrock breccia, Type 10a (Sample 158-957H-5N-2, Piece 1C, 19–25 cm).

$\mu\text{m}$  and  $>420 \mu\text{m}$ ) fractions. Analyses of the 63–420  $\mu\text{m}$  and  $<63 \mu\text{m}$  fractions by ASV indicate a uniform bulk gold content of about 3 ppm Au. Samples of the fine- and medium-sized fractions are deficient in S compared with the total metal concentrations.

#### *Porous Nodular Pyrite Breccia (Type 6a)*

Only one sample of this rock type (Sample 158-957H-1N-1, Piece 13) was analyzed. It has high Fe, Cu, and S concentrations similar to Type 6 and 6b samples from the TAG-1 area (see Table 8, Chapter 7, this volume). Its high S content reflects the abundance of anhydrite as well as sulfide minerals.

#### *Nodular Pyrite-Silica Breccia (Type 9b)*

Two samples of nodular pyrite-silica breccia from the deeper part of Hole 957H were analyzed (Samples 158-957H-5N-1, Piece 6 and 6N-1, Piece 3). Both samples analyzed were nodules and may contain larger amounts of chalcopyrite associated with coatings/veins on the exteriors of clasts. The Fe, Cu, and S contents of the two samples differ significantly from each other, but the trace element contents, such as Pb, Ag, and Cd, are very low. Sample 158-957H-5N-1 (Piece 6) has a moderately high Fe content and low Cu and Zn contents. The metal and sulfur contents of this sample are within the range of Type 9a samples from the TAG-1 area (see Table 8, Chapter 7, this volume). However, Sample 158-957H-6N-1 (Piece 3) has lower Fe and much higher Cu contents compared to Sample 158-957H-5N-1, a difference reflected in the higher proportion of chalcopyrite in the analyzed piece. However, the amounts of chalcopyrite that correspond to measured Cu values are consistently greater than all visual estimates of chalcopyrite, suggesting either that visual estimates of chalcopyrite are too low, or that differences between chemical compositions and visual estimates reflect the heterogeneous nature of these breccias.

#### *Chemical Variations Along a Stratigraphic Profile in the TAG-2 Area*

Variations in metals and sulfur contents with depth are plotted in Figure 30. Metal concentrations, except for Fe, increase near the sur-

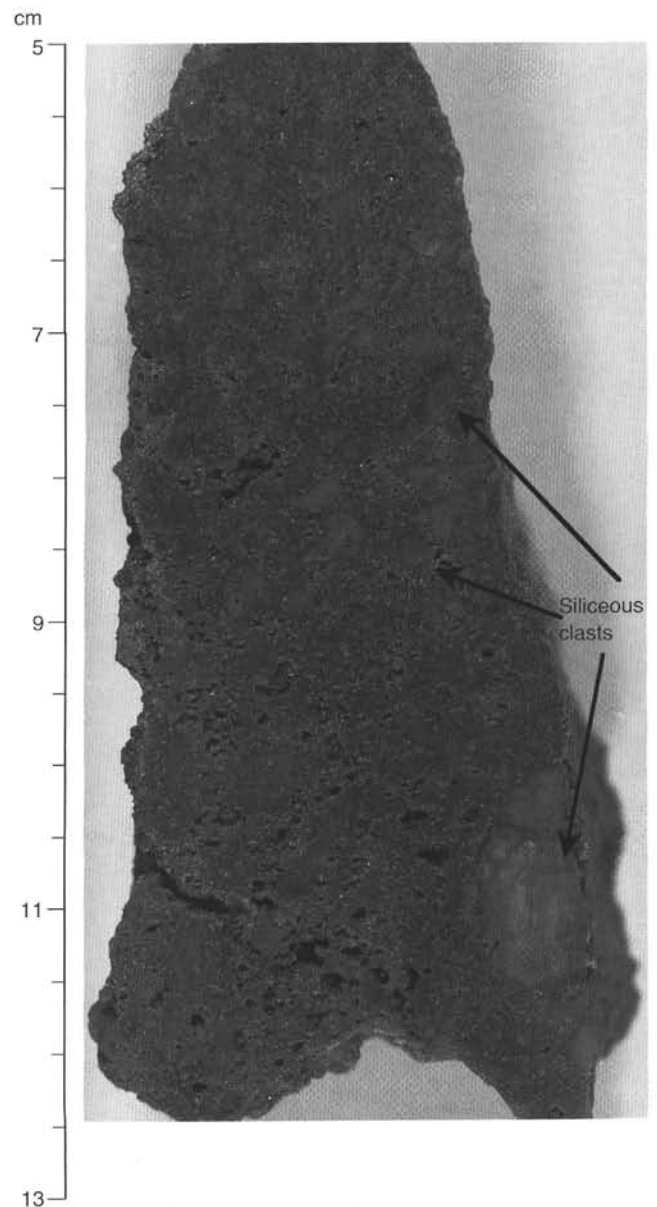


Figure 28. Dark gray chert in Sample 158-957N-1W-1 (Piece 2, 5–13 cm) (Type 2), composed of 10% fine-grained pyrite disseminated in very fine-grained silica, and light gray silica clasts.

face. High metal contents other than Fe were also observed in surface samples collected by a submersible in the Kremlin area, and were suggested to be the result of mineral deposition from white smoker fluids (Tivey et al., 1995). Samples deeper than 9.3 mbsf have low metal concentrations similar to the samples in TAG-1 area. Likewise metal ratios (Cu/Fe, Zn/Fe, and Zn/Cu) are also similar to samples from the TAG-1 area. This indicates that processes responsible for the enrichment of Cu, Zn, Pb, Ag, and Cd (e.g., mineral deposition from white smoker fluids) occur only in the near-surface part (upper 10 m) of the Kremlin area. Below this zone, samples from the Kremlin area are chemically similar to those in the TAG-1 area.

#### **Calculated Modal Composition of Sulfides**

To determine the presence of minerals other than sulfides, mineralogical compositions of samples are calculated assuming only pure pyrite, chalcopyrite, sphalerite, anhydrite, and hematite are present in

samples. The method of calculation is as follows: (1) Zn is used to make pure sphalerite, (2) Cu is used to make pure chalcopyrite, (3) remaining Fe and S are used to make pyrite. If there is excess S, then it is assumed to be present as anhydrite; if there is excess Fe, then it is assumed to be present as hematite.

The results of these calculations are shown in Table 5 and indicate the presence of hematite and absence of anhydrite in all fractions. The hematite abundance is higher in the finer fractions. Chalcopyrite is enriched in the finer fraction and sphalerite in the medium and coarser fraction.

Visual core descriptions suggested that Fe-oxides (65 vol%) together with gray and red chert (30 vol%) comprise the major minerals of this sample with only minor contributions of sulfides (pyrite 5 vol%). The significant difference in the abundance of sulfide minerals between visual description and chemical analyses is probably caused by either the fine grain size of the sulfide minerals or the oxide coating of the sulfide grains, which make visual observations difficult.

### Summary

On the surface of the mound, the Kremlin area (TAG-2) differs from areas near the Black Smoker Complex in terms of both the composition of venting fluid (copper poor and zinc rich) relative to fluids sampled from Black Smoker Complex chimneys (Edmond et al., 1995) and the mineralogy and geochemistry of hydrothermal precipitates (zinc-rich relative to samples recovered from elsewhere on the mound surface; Tivey et al., 1995). Cores recovered from Holes 957A, 957B, 957H, and 957N provide information on lithologies present at depth below the Kremlin area. The drill cuttings from the top of the first core drilled at Hole 957B, and the small pieces of porous massive sphalerite from that core and from Core 158-957A-3X, are the only zinc-rich materials recovered from beneath the Kremlin area. The small size of the individual samples recovered (pieces less than 5 cm in diameter), and the presence of clasts of porous pyrite and chert in a chert matrix, and of clasts of chert in porous pyrite samples, are consistent with Hole 957A (0–15 mbsf) intersecting a zone of chert-sulfide breccia. Clasts of red chert are present in porous massive pyrite, which in turn is present as clasts in chert-sulfide breccia. The porous massive pyrite samples exhibit primary textures and only partial recrystallization. Samples of porous massive pyrite ± chalcopyrite, cut by small veins of anhydrite, and small pieces of red chert, were recovered in the first core from Hole 957H. Chalcedony present in chert samples from the shallow levels (<19.9 mbsf) of Holes 957A, 957B, 957H, and Hole 957N may be recrystallized amorphous silica. The gray silica sample from Core 158-957A-3X shows filamentous texture and no evidence of recrystallization. This filamentous silica is similar to silica observed in the outer portions of the white smoker chimneys at the mound surface (Tivey et al., 1995) and may have formed there. Given the lack of stratigraphic control, it is possible that the small pieces of porous massive sphalerite found in

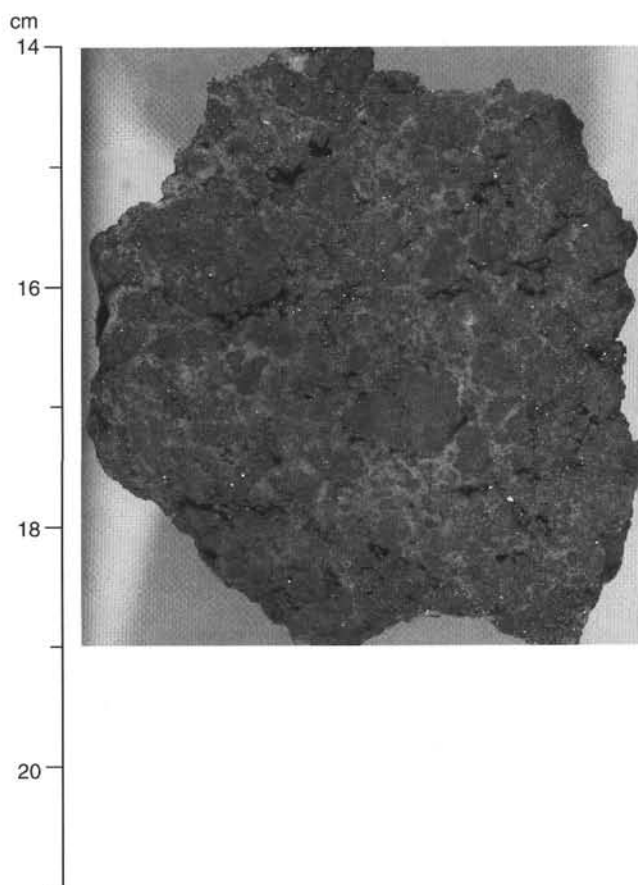


Figure 29. Pyrite-silica-anhydrite breccia in Sample 158-957N-1W-1 (Piece 3, 14–21 cm) (Type 8), containing 70 vol% very fine-grained silica intermixed with minor anhydrite as matrix, and 20 vol% fine-grained pyrite as nodular clasts and disseminated in the matrix.

Holes 957A and 957B originated at or near the surface of the mound, where active white smokers are present. The recovery of massive pyrite in Core 158-957B-1R indicates that such material is present within 9.9 m of the surface at this location (Table 2). Similar but somewhat finer grained material was recovered in cores from shallow levels in Hole 957H, primarily as large clasts in porous nodular pyrite breccia.

The first occurrence of basaltic material is at similar depths in cores from both Hole 957B (between 19.9 and 29.61 mbsf) and Hole 957H (between 26.7 and 31.2 mbsf). In cores from Hole 957H, basal-

Table 4. AAS, CHNS, and ASV analyses of sulfide samples from Hole 957H.

Core, section, interval (cm)	Size fraction or piece no.	Type	Rock type	Fe (wt%)	Zn (wt%)	Cu (wt%)	Pb (ppm)	Ag (ppm)	Cd (ppm)	S (wt%)	Au (ppb)
158-957B-											
1R-1	>420 $\mu$ m	1	Drill cuttings, Fe-oxides	20.1	2.730	8.23	200	146	99.8	23.5	ND
1R-1	63–420 $\mu$ m	1	Drill cuttings, Fe-oxides	32.7	3.020	13.70	393	155	99.0	36.4	ND
1R-1	<63 $\mu$ m	1	Drill cuttings, Fe-oxides	31.2	1.370	13.40	270	109	46.3	33.2	3000
158-957H-											
1N-1	13	6a	Porous, nodular pyrite breccia	30.6	0.014	6.70	ND	4.6	<0.1	43.8	ND
5N-1	6	9b	Nodular pyrite-silica breccia	32.4	0.020	0.51	4	4.4	<0.1	39.9	ND
6N-1	3	9b	Nodular pyrite-silica breccia	27.5	0.015	4.11	5	4.9	<0.1	33.2	ND

Note: ND = not determined.

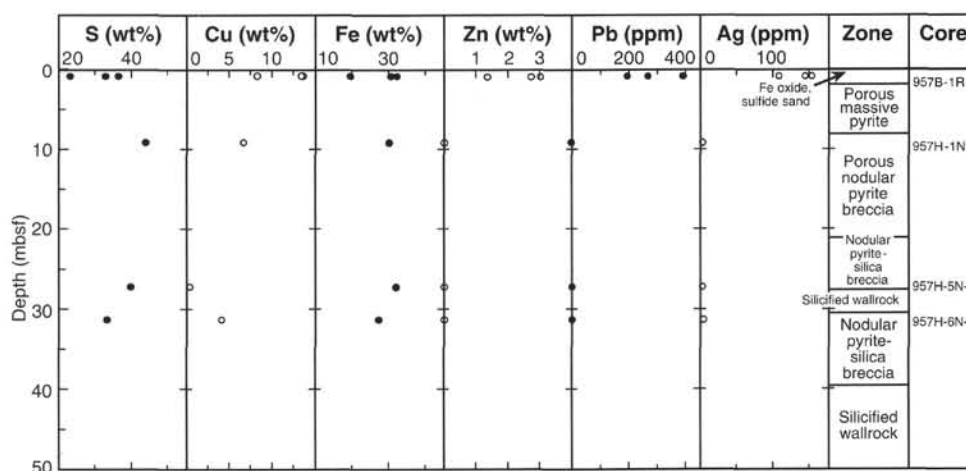


Figure 30. Depth profile of the concentrations of S, Cu, Fe, Zn, Pb, and Ag in the TAG-2 (Kremlin) area.

Table 5. Modal composition of sulfide samples of TAG-2 (Kremlin) area recalculated from chemical analyses.

Core, section, interval (cm)	Size fraction or piece no.	Pyrite (wt%)	Sphalerite (wt%)	Chalcopyrite (wt%)	Anhydrite (wt%)	Hematite (wt%)	Others (%)	Total sulfide
158-957B-1R-1	>420 $\mu\text{m}$	26.0	4.1	23.8	0.0	1.1	45.1	53.8
1R-1	63–420 $\mu\text{m}$	39.5	4.5	39.6	0.0	3.2	13.2	83.5
1R-1	<63 $\mu\text{m}$	35.5	2.0	38.8	0.0	4.1	19.6	76.3
158-957H-1N-1	13	53.1	0.0	19.4	36.8	0.0	-9.3	72.5
5N-1	6	68.6	0.0	1.5	11.6	0.0	18.3	70.1
6N-1	3	51.3	0.0	11.9	6.9	0.0	29.9	63.2

tic material is present as clasts in nodular pyrite-silica breccia and silicified basalt breccia. In Hole 957B, chloritic mud and single pieces of altered basalt were recovered in cores, not clasts in silicified breccias. The presence of these basalt pieces may indicate uppermost basement, or a portion of a basaltic flow. Silicified wallrock breccias recovered from similar depths in Hole 957H may also represent uppermost basement that has been brecciated and silicified (see "Hydrothermal Alteration" section, this chapter). Recovered cores from below 26.7 mbsf in Hole 957H consist of nodular pyrite-silica breccias, pyrite-silica breccias, and silicified wallrock breccias. These breccias are similar to those recovered in cores from Holes 957C and 957E in the TAG-1 area, below depths of 40.2 mbsf; however, they exhibit trace amounts of hematite and coarser grained anhydrite lining vugs. At the TAG-1 site, such samples are interpreted as pieces of the present stockwork zone. At TAG-2, as at TAG-1, portions above this stockwork contain greater amounts of anhydrite. Although the abundance of anhydrite in cores from Hole 957H is less than that observed in cores from Hole 957C in the TAG-1 area, the overall distribution, from more abundant at upper levels decreasing to trace amounts in samples recovered from the stockwork zone, is similar.

## HYDROTHERMAL ALTERATION

Various types of altered basaltic material were recovered from Holes 957B, 957H, and 957N in the Kremlin area of the TAG mound (TAG-2 area; see Fig. 3, Chapter 1, this volume). Altered basaltic material in Hole 957H occurs as variable amounts of silicified basalt and hyaloclastite clasts locally in pyrite-silica breccia from 26.7 mbsf to the bottom of the hole at 54.5 mbsf, and in silicified wallrock breccias at 27.6–31.2 mbsf (Section 158-957H-5N-2) (Fig. 3). In Hole

957N, clasts of silicified basalt occur in the 50 cm of pyrite-silica and pyrite-silica-anhydrite breccias recovered in a wash core from the interval 0–42.2 mbsf. Altered basaltic rocks from Hole 957B were recovered from the interval 19.9–29.6 mbsf (Cores 158-957B-4R and 5B) (Fig. 2). These include a pillow-rim breccia, a hydrothermal chert containing chloritized glass fragments, and underlying dark gray, slightly altered basalt.

The silicified basalt clasts in the breccias of Hole 957N consist of 3- to 15-mm rounded, buff to gray fragments, which are silicified and contain abundant disseminated pyrite, as well as gray to buff chlorite(?). Some clasts are totally replaced by gray quartz plus disseminated pyrite. These clasts occur in matrices of gray quartz plus pyrite  $\pm$  white anhydrite (see "Sulfide Petrology and Geochemistry" section, this chapter), and are identical to those occurring in other cores from the TAG mound (e.g., from the upper parts of Hole 957H in the TAG-2 Kremlin area; see below).

The silicified basalt clasts in the pyrite-silica breccias and in the silicified wallrock breccias of Hole 957H are gray to buff, 2-mm to 3-cm, rounded to angular fragments in a fine-grained matrix of gray quartz plus pyrite (Fig. 26). Pyrite in the matrix is present as 0.1- to 1-cm grains and rounded aggregates. The basalt clasts themselves are composed of a buff phyllosilicate plus quartz, and contain variable amounts of fine-grained pyrite replacing plagioclase microlites and disseminated in the groundmass. The clasts are replaced by quartz to various extent, with gray portions that are more intensively silicified. These textures are similar to those observed in cores from the eastern side of the Black Smoker Complex (TAG-1 area, Holes 957C and 957E). Silicified basalt clasts occur in the pyrite-silica breccias and silicified wallrock breccias of Hole 957H at 26.7–27.2, 40.2–44.7, and 44.7–54.5 mbsf (Sections 158-957H-5N-1, Pieces 3, 5, and 7; 8N-1, Pieces 6 and 8; and 9X-1, Pieces 1 and 2). These breccias locally con-

tain large (2–5 cm) clasts of white to gray quartz with disseminated pyrite (Sections 158-957H-5N-1 and 5N-2), one containing altered glass fragments and one partly stained red by iron oxides/oxyhydroxides. Although only small numbers of silicified basalt clasts can be identified in the pyrite-silica breccias from Hole 957H, other siliceous clasts and matrix material in these rocks could also be totally silicified basaltic material, now beyond recognition in hand specimen, as was observed in cores from Holes 957C and 957E.

A thin section of silicified wallrock breccia from Hole 957H (Sample 158-957H-5N-2, Piece 3A, 58–62 cm) is similar to those of breccias recovered from the eastern side of the Black Smoker Complex (see Figs. 82–83, Chapter 7, this volume), and reveals relict sub-variolitic texture, with plagioclase microlites replaced by brown to tan clay (chlorite?) and quartz. The fine-grained, feathery to sheaf-like interstitial material is replaced by tan to brown phyllosilicate (chlorite? or illite?), and micrometer-sized gray granules may be titanite. The 150- $\mu\text{m}$ -sized olivine phenocrysts are pseudomorphed by quartz with red iron oxide/oxyhydroxide inclusions. Pyrite is abundant as disseminated 5- to 100- $\mu\text{m}$  grains, and basaltic clasts are cut by a network of 50- to 600- $\mu\text{m}$  quartz  $\pm$  pyrite veinlets. Where the clasts are intensively veined, the basalt is highly silicified and pyritized. “Dirty”-looking quartz is common in the veins and contains abundant trails of inclusions of fluid and clays (and leucoxene?), which apparently mimic the sub-variolitic texture of the precursor basalt. The 10- to 100- $\mu\text{m}$  patches of clay-rich quartz in the quartz matrix are relics of highly altered basalt clasts. The matrix otherwise consists of subhedral to euhedral, zoned quartz crystals and is pyrite rich (up to 85% pyrite), with late anhydrite locally filling pore space.

The silicified hyaloclastite from Hole 957H consists of 1- to 5-mm, angular fragments of altered basaltic glass in a matrix of fine-grained, gray quartz (Fig. 31). The glass fragments are altered to green chlorite and a white phyllosilicate, commonly in concentric bands. The glass shards are also variably silicified and replaced by fine-grained pyrite. Hyaloclastite is present in a continuous, 20-cm-thick interval near the top of the silicified wallrock breccia of Section 158-957H-5N-2 (Pieces 1A–C), and in 1- to 5-mm clasts in the pyrite-silica breccias of Sections 158-957H-5N-1 (Piece 5C) and 158-957H-8N-1 (Pieces 6 and 8).

The silicified wallrock breccia from Hole 957H (Section 158-957H-5N-2; 27.6–31.2 mbsf) consists mainly of 2- to 20-mm, round to angular clasts of gray to buff silicified basalt in a matrix of dark gray quartz plus pyrite. Pyrite clasts are common, and pyrite is also present as matrix material cementing pyritic and siliceous clasts. Pyrite is much more abundant as both matrix and clasts than in siliceous wallrock breccias from Holes 957C and 957E. Round, light gray quartz clasts, with disseminated pyrite and red iron oxide/oxyhydroxide-stained patches, are also present, and range up to 5 cm across in Section 158-957H-5N-2 (Piece 3B). Silicified hyaloclastite occurs in a 20-cm interval near the top of Section 158-957H-5N-2 (in Pieces 1A–C), and locally in clasts elsewhere in Section 158-957H-5N-2.

Although veins are relatively rare in these rocks, a generalized vein sequence was observed. First, quartz formed in veins and in silicified basalt clasts, then pyrite formed as linings of pores and in veins, and finally late anhydrite formed in veins cutting earlier veins and filling remaining pore spaces. For example, anhydrite-filled vugs lined by pyrite are common in Section 158-957H-5N-2. Pyrite also formed relatively early in these rocks, as the silicified basalt fragments also contain abundant disseminated pyrite, and pyrite clasts are commonly cemented by pyrite and later anhydrite. Minor pyrite and chalcopyrite are also associated with some anhydrite veins in these rocks (see “Sulfide Petrology and Geochemistry” section, this chapter).

In Hole 957B, the upper 30 cm of Core 158-957B-4R consists of a pillow-rim breccia, with centimeter-sized pieces of altered crystalline and glassy basalt in a matrix of red mud, which is made up of hematite, chlorite, and quartz. The crystalline basalt fragments are grayish red and completely replaced by yellow phyllosilicates and he-

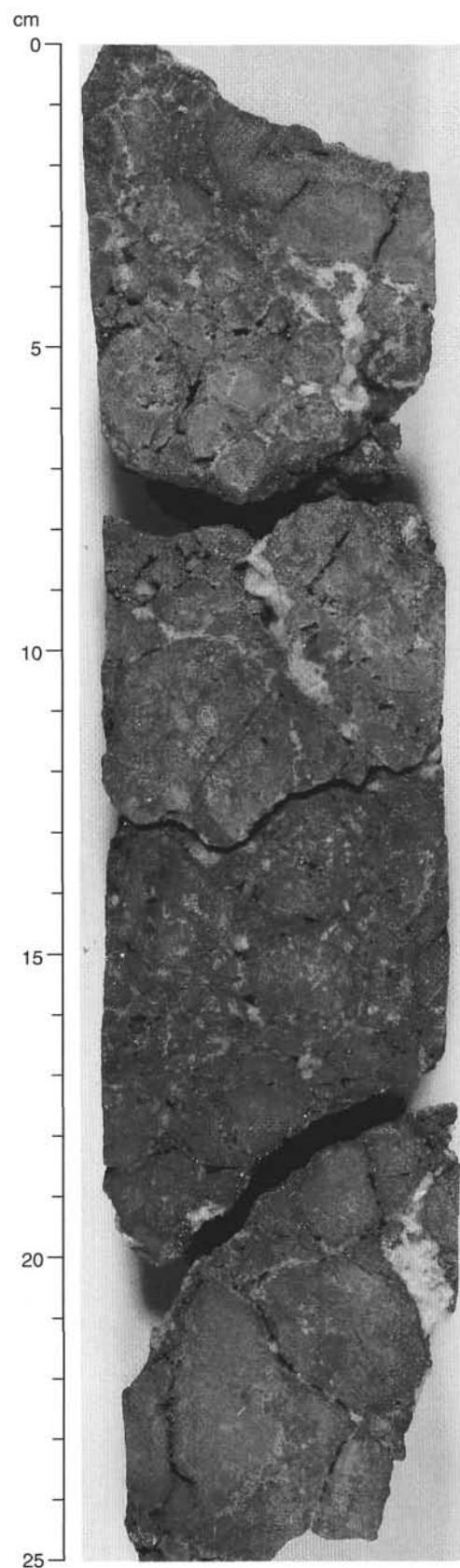


Figure 31. Silicified wallrock breccia, with silicified hyaloclastite at 0–19 cm. White veins are late anhydrite. Sample 158-957H-5N-2 (Pieces 1A–C, 0–25 cm).

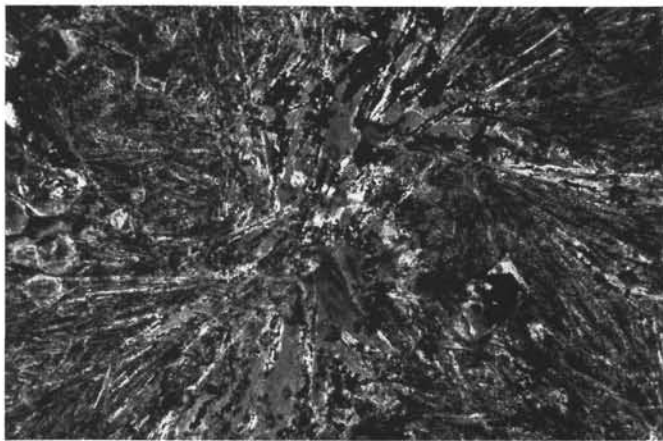


Figure 32. Subvariolitic texture in the least altered inner part of altered basalt, Sample 158-957B-4R-1 (Piece 9, 51–54 cm). Unaltered plagioclase microlites (white), glassy groundmass (light gray), and smectite and iddingsite pseudomorphs after olivine phenocrysts in a glomerophytic aggregate (left). Smectite and iddingsite pseudomorph after a single olivine phenocryst (lower center right). Uncrossed polars, field of view = 1.5 mm.

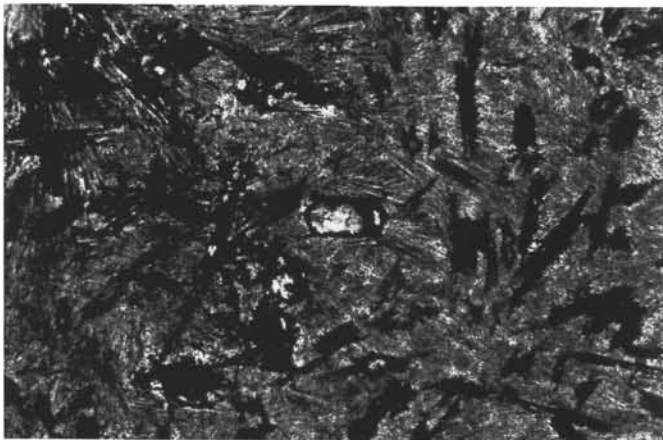


Figure 34. Subvariolitic texture in the red alteration halo of the outer rim of a basalt in Sample 158-957B-4R-1 (Piece 9, 51–54 cm).  $\text{Fe}(\text{OH})_n$  pseudomorphs after plagioclase microlites are scattered in the altered subvariolitic groundmass. At center is an  $\text{Fe}(\text{OH})_n$  pseudomorph after an isolated olivine crystal (some material lost during thin-sectioning). Uncrossed polars, field of view = 1.5 mm.

matite. The basalt fragments exhibit complex, millimeter-wide, red and brown alteration halos along formerly exposed surfaces. Basaltic glass fragments are blue gray and completely altered to chlorite, as determined by X-ray diffraction analysis (see below).

Also included in Core 158-957B-4R is a 1 × 3 cm piece of red and gray chert (Sample 158-957B-4R-1, Piece 5, 43–48 cm). This fragment consists of several 1- to 5-mm clasts of chloritized glass and hematite cemented by fine-grained gray quartz with disseminated pyrite, an unidentified phyllosilicate, and iron oxides/oxyhydroxides (see “Sulfide Petrology and Geochemistry” section, this chapter).

In the lowermost portion of Hole 957B, the bottom three pieces of Core 158-957B-4R and the two pieces from Core 158-957B-5B are mainly dark gray, slightly altered, subvariolitic basalt, with 2- to 3-mm wide, more intensively altered, red-brown alteration halos along inferred former fractures or exposed surfaces. Olivine phenocrysts

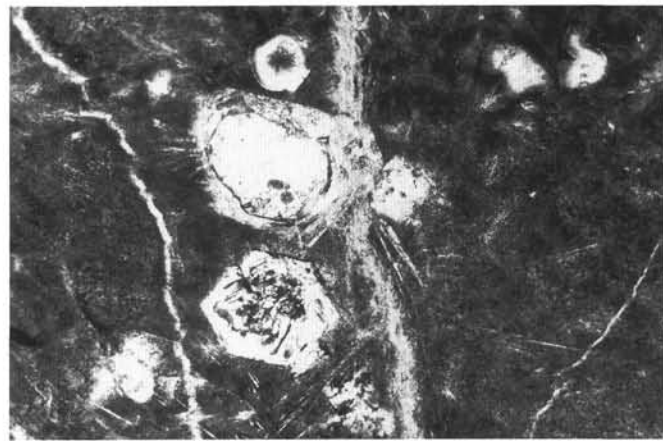


Figure 33. A 0.10- to 0.15-mm-thick smectite vein crossing the least altered inner part of a subvariolitic basalt in Sample 158-957B-4R-1 (Piece 9, 51–54 cm). Two smectite pseudomorphs after olivine crystals also present (center). The largest olivine crystal is intersected by the vein and contains a large olivine relic. One vesicle (near top) and two vugs (upper right corner) are filled with smectite. Open crack at left. Uncrossed polars, field of view = 1.5 mm.

are partially replaced in Core 158-957B-5B and completely replaced in Core 158-957B-4R by yellow phyllosilicate (smectite?) and iron oxyhydroxides and/or oxides (Fig. 32). Phyllosilicate (smectite?) and iron oxyhydroxides also fill vesicles (0.2–1.6 mm diameter) and veins (~0.1 mm in width) (Fig. 33). In the red alteration halos, the rock is completely altered to phyllosilicate (smectite?) and iron oxyhydroxides and/or oxides but the subvariolitic texture is preserved (Figs. 32, 34).

Because the shipboard X-ray diffractometer did not work during Leg 158, chemical analysis by X-ray fluorescence was used to help identify the red mud from the pillow-rim breccia in Sample 158-957B-4R-1, 1–3 cm. The air-dried bulk sample was gently disaggregated with an agate mortar and pestle, and dispersed in 100 mL of nanopure water using ultrasonic agitation for 10 min. The resulting suspension was allowed to settle according to Stokes Law, and the <4- $\mu\text{m}$  fraction siphoned off, centrifuged, and oven-dried at 60°C. This <4- $\mu\text{m}$  fraction was analyzed using standard shipboard X-ray fluorescence techniques, and the results are given in Table 6.

The chemical composition of Sample 158-957B-4R-1, 1–3 cm, for the <4- $\mu\text{m}$  fraction is essentially identical to chlorite (Deer et al., 1966). The high  $\text{TiO}_2$  content (2.1 wt%) of the <4- $\mu\text{m}$  fraction of Sample 158-957B-4R-1, 1–3 cm, suggests that the mud matrix of the breccia is hydrothermally altered basaltic material, rather than a purely hydrothermal precipitate. Some of this breccia matrix may be ground-up chloritized hyaloclastite, the intact relics of which are observed in some of the breccia clasts and in interval 158-957B-4R-1, 25–30 cm. The chloritic material exhibits increased  $\text{MgO}$ ,  $\text{Fe}_2\text{O}_3$ , and  $\text{Al}_2\text{O}_3$  and decreased  $\text{CaO}$  and  $\text{SiO}_2$  relative to the analyzed basalt sample from the same core (Sample 158-957B-4R-1, Piece 8; see Table 6). Shore-based X-ray diffraction analysis indicates that Samples 158-957B-4R-1, 10–15, 16–24, and 30–38 cm, are made up of various proportions of chlorite, quartz, and hematite.

### Interpretation

The chloritized glass fragment in red and gray chert, the chloritized basaltic material from the base of Hole 957B, and the presence of hematite are evidence for hydrothermal activity. The presence of chlorite implies temperatures greater than 200°–250°C. In contrast, the presence of (tentatively identified) smectite and only slight alteration of the dark gray basalt fragments are compatible with typical low-temperature alteration of the uppermost oceanic crust. Mineral

**Table 6. X-ray fluorescence chemical analyses of the <4- $\mu$ m size fraction of the mud matrix of Sample 158-957B-4R-1, 1–3 cm.**

Core, section, interval (cm)	SiO <sub>2</sub>	TiO <sub>2</sub>	Al <sub>2</sub> O <sub>3</sub>	Fe <sub>2</sub> O <sub>3</sub>	MnO	MgO	CaO	Na <sub>2</sub> O	K <sub>2</sub> O	P <sub>2</sub> O <sub>5</sub>	LOI
158-957B- 4R-1, 1–3	32.4	2.14	16.3	24.4	0.067	24.9	0.093	<0.1	0.015	0.033	11.15
4R-1, 1–3	31.9	2.10	16.0	23.7	0.065	24.5	0.077	<0.1	0.014	0.031	11.15
Chlorite	27.6	0.22	22.5	12.1	0.020	24.3	0.000	0.17	0.060	—	13.30

Notes: Analysis was performed in duplicate. Chlorite analysis from altered basalt (Deer et al., 1966) for comparison. Compositions in weight percent. LOI = loss on ignition.

identifications in the altered basalts are only tentative, however, and alteration temperatures could have been higher (up to 200°C?) to produce smectite in the rocks. The slightly altered, dark gray basalt is interpreted as the uppermost basement in the Kremlin area; however, as only a small amount of basalt was recovered, it is possible that this material represents a portion of a basaltic flow. Silicified basaltic material was recovered from similar depths in Holes 957B (19.9–29.6 mbsf) and 957H (below 26.7 mbsf). Although rocks are only locally identified as silicified wallrock breccias below 26.7 mbsf in Hole 957H, much of the pyrite-silica breccia interspersed with these rocks below 26.7 mbsf in Hole 957H could contain totally silicified basaltic material, in which case basement may have originally begun at similar depths in both holes. Whatever the case may be, the effects of hydrothermal activity within the margins of the mound and associated uppermost basement are heterogeneous on a scale of meters or less. The silicified stockwork zone, as penetrated by Hole 957H below 26.7 mbsf, extends within about 30 m of the edge of the mound, at least near the surface, and it is likely that there is a relatively abrupt transition to low-temperature alteration that is more typical of uppermost oceanic basement surrounding the mound.

Alteration of the basaltic material in Hole 957H is generally similar to that occurring in the silicified wallrock zones of Holes 957C and 957E from the eastern side of the Black Smoker Complex (i.e., the uppermost siliceous stockwork zone). Vein sequences in the silicified wallrock breccias of the two areas are also similar in general. Both these observations suggest similar alteration processes in the uppermost stockwork zone from the inner and outer portions of the mound.

## IGNEOUS PETROLOGY AND GEOCHEMISTRY

Basement samples are fragments of very fine-grained, aphyric to sparsely olivine phryic, pillow basalt. A piece-by-piece description of these samples appears in Table 7. These include a pillow-rim breccia in the upper 43 cm of Core 158-957B-4R (19.9–29.6 mbsf), altered basalt fragments in the bottom three pieces of Core 158-957B-4R, and two pieces from Core 158-957B-5B. In the red brown to light gray pillow-rim breccia from Section 158-957B-4R-1 (0–30 cm, Pieces 1–4), centimeter-sized pieces of altered crystalline and glassy sparsely phryic olivine basalt occur in a matrix of metalliferous mud. Red brown to dark gray aphyric basalt fragments (Intervals 158-957B-4R-1, Pieces 6–8, and 5B-1, Pieces 1–2) exhibit rare olivine phenocrysts in a microcrystalline groundmass containing plagioclase microlites. These samples have been variably altered as described in the “Hydrothermal Alteration” section (this chapter).

Samples 158-957B-4R-1 (Piece 2, 19–21 cm), 4R-1 (Pieces 7 and 8), and 5B-1 (Piece 2) exhibit euhedral olivine phenocrysts 0.07 to 0.55 mm in length, as observed in thin sections. Euhedral and bow-tie plagioclase microlites 0.1 to 1.0 mm in length occur in a microcrystalline, subvolcanic groundmass in these three samples. A typical subvolcanic texture from Sample 158-957B-4R-1 (Piece 7) is shown in Figure 26. Only Sample 158-957B-4R-1 (Piece 7) contains unaltered olivine in the cores of the phenocrysts (see Fig. 31) and unaltered plagioclase microlites. Rounded to elongated vesicles com-

prise 1% to 2% of these samples and are 0.1 to 1.6 mm in diameter. One segregation vesicle occurs in Sample 158-957B-4R-1 (Piece 7).

Whole-rock geochemistry was determined for Sample 158-957B-4R-1 (Piece 8), and the major and trace element compositions are listed in Table 8. This basalt exhibits a Mg# of 61.7 and contains 1.63 wt% TiO<sub>2</sub> and 2.29 wt% Na<sub>2</sub>O.

## PHYSICAL PROPERTIES

### Introduction

Physical properties measurements were made on rock samples in cores recovered from the Kremlin area in Holes 957B and 957H. Depending on the available material (minicores or fragments), an effort was made to sample representative lithologies for each section recovered. However, some of the rock types sampled in the TAG-2 area are very heterogeneous sulfide breccias, so that the physical properties measured may not necessarily represent the overall properties of the rock classification from which the sample was extracted. Results are presented according to the type of measurements made for each hole. Physical properties were measured on rock samples, as follows:

Hole 957B: Fe-oxides and sulfide sand (drill cuttings), one sulfide fragment, and two altered basalt fragments.

Hole 957H: two sulfide minicores, six sulfide fragments, and two half-round slabs.

### Hole 957B

Index properties were measured on materials in cores recovered from Hole 957B, as follows:

1. Section 158-957B-1R-1 (1.7 m interval at top): Water-saturated drill cuttings consisting of red mud incorporating sulfide grains, fragments of red and gray chert, and massive pyrite clasts classified as drill cuttings comprised of Fe-oxides and sand-sized sulfide grains (Table 2, back pocket). One sample (Table 9) yielded a very high porosity value of 61.6%, associated with a low bulk density of 1.86 g/cm<sup>3</sup>.
2. Section 158-957B-1R-2: A fragment of porous massive sphalerite (Table 9), has a high porosity of 20.9% and a bulk density of 2.61 g/cm<sup>3</sup>. This specimen (Sample 158-957B-1R-2, 12–14 cm) is probably part of a white smoker chimney (see “Sulfide Petrology and Geochemistry” section, this chapter).
3. Sections 158-957B-4R-1 and 5B-1: At a depth of 20.1–29.6 mbsf, two altered basalt fragments, one from each core, exhibit high porosities (15.7% and 18.6%) and low wet bulk densities (2.25 and 2.43 g/cm<sup>3</sup>) (Table 9).

### Hole 957H

Physical properties measurements were made on a variety of samples (two minicores, six fragments, and two half-rounds) selected as representative from seven of the nine cores that recovered predomi-

Table 7. Igneous lithology for TAG-2 area.

Core, section, interval (cm)	Piece no.	Piece depth (mbsf)	Unit	Lithology	Contact	Olivine		Average		Phenocryst habit	Color
						Min. (%)	Max. (%)	gs-ph (mm)	gs-gm (mm)		
158-957B-											
4R-1, 0-16	1	19.90	1	Sparsely olivine phyric pillow rim breccia	No contact observed	1	3	0.5	0.7	Euhedral	Brown gray
4R-1, 16-25	2	20.06	1	Sparsely olivine phyric pillow rim breccia		1	3	0.5	0.7	Euhedral	Brown gray
4R-1, 25-39	3	20.15	1	Sparsely olivine phyric pillow rim breccia		1	3	0.5	0.7	Euhedral	Brown gray
4R-1, 39-43	4	20.29	1	Sparsely olivine phyric pillow rim breccia		1	3	0.5	0.7	Euhedral	Brown gray
4R-1, 43-47	5	20.33	1	Sparsely olivine phyric pillow rim breccia	No contact observed				0.7		Red brown
4R-1, 47-50	6	20.37	2	Aphyric basalt		0	1	0.5	0.7	Euhedral	Dark gray
4R-1, 50-55	7	20.40	2	Aphyric basalt		0	1	0.5	0.7	Euhedral	Dark gray
4R-1, 55-60	8	20.45	2	Aphyric basalt		0	1	0.5	0.7	Euhedral	Dark gray
5B-1, 0-3	1	29.60	2	Aphyric basalt					0.5		Red gray
5B-1, 3-9	2	29.63	2	Aphyric basalt	No contact observed				0.5		Red gray

Table 8. Whole-rock XRF basalt chemistry of Sample 158-957B-4R-1 (Piece 8).

	Average	1 SD
Major elements (wt%):		
SiO <sub>2</sub>	50.58	0.07
TiO <sub>2</sub>	1.63	0.02
Al <sub>2</sub> O <sub>3</sub>	15.00	0.04
Fe <sub>2</sub> O <sub>3</sub>	10.88	0.04
MnO	0.17	0.01
MgO	8.86	0.03
CaO	10.59	0.05
Na <sub>2</sub> O	2.29	0.07
K <sub>2</sub> O	0.08	0.00
P <sub>2</sub> O <sub>5</sub>	0.15	0.00
Total	100.22	
LOI	2.48	
FeO <sup>++</sup>	9.79	
Mg#	61.73	0.07
FeO/MgO	1.10	0.00
CaO/Al <sub>2</sub> O <sub>3</sub>	0.71	0.00
Trace elements (ppm):		
V	283	
Cr	338	
Ni	172	
Cu	80	
Zn	86	
Rb	2	
Sr	111	
Y	34	
Zr	80	
Nb	3	
Ba	13	
Ce	BDL	

Notes: Major element composition represents average of three replicate analyses. FeO<sup>++</sup> = total iron as FeO. Mg# = 100 × (Mg/(Mg+ΣFe)). SD = standard deviation, LOI = loss on ignition, and BDL = below detection limit.

nantly sulfides at Hole 957H. Core 158-957H-4N had no recovery and another core (158-957H-7N) recovered only a few pieces that were unsuitable for physical properties measurements. Results are presented according to the type of measurement.

#### Multisensor Track

A cumulative length of 42 cm comprising seven segments of Sections 158-957H-5N-1 and 5N-2 was sufficiently intact for multisensor track (MST) measurements, as shown in Figure 35. After correcting the raw data of wet bulk density measurements by the MST GRAPE device for deviation of core diameter (56–57 mm for Core 158-957H-5N) from full diameter (66.1 mm; Fig. 7, Chapter 5, this volume), the values (3.89 g/cm<sup>3</sup> for 57 mm diameter of Section 158-957H-5N-1, and 4.36 g/cm<sup>3</sup> for 56-mm diameter of Section 158-957H-5N-2) are consistent with discrete index properties measurements (3.70 and 4.33 g/cm<sup>3</sup>) on minicores from corresponding core intervals (Table 9, Samples 158-957H-5N-1, 33–35 cm, and 5N-2, 29–31 cm).

A small range of values (7–10.5 cps) exists for natural gamma radiation. These values are variable within the depth interval measured, increasing from 7.0 to 9.5 cps between 26.7 and 27.1 mbsf, decreasing from 9.5 to 7 cps between 27.1 and 27.8 mbsf, and increasing from 7.0 to 10.5 cps between 27.8 and 27.9 mbsf (Fig. 35). The values for volume magnetic susceptibility (4 to 11 × 10<sup>-5</sup> SI) show a similar variation with depth to that described for the natural gamma radiation within the same interval (Fig. 35). The MST values of volume magnetic susceptibility agree with the values measured on the two minicore samples (158-957H-5N-1, 33–35 cm, and 5N-2, 29–31 cm) at corresponding depths (27.03 and 27.89 mbsf; see “Paleomagnetism” section, this chapter).

#### Index Properties

Index properties for seven of the eight samples measured exhibit a range of values for bulk densities (3.63–4.33 g/cm<sup>3</sup>), grain densities (3.81–4.69 g/cm<sup>3</sup>), and porosities (6.38–11.52%) (Table 9). The uppermost sample of a porous massive pyrite (158-957H-1N-1, 19–21 cm) is exceptional for relatively low bulk density (3.27 g/cm<sup>3</sup>) and high porosity (21.53%) values (Table 9, Figs. 36–37). No trends for these properties are apparent over the depth range sampled from Hole 957H (8.9–44.9 m; Fig. 36). Minicore Sample 158-957H-5N-1, 33–35 cm, was extracted from a nodular pyrite-silica breccia. Minicore Sample 158-957H-5N-2, 29–31 cm, occurs within a section of silicified wallrock breccia. However, the minicore interval is predominantly pyrite with a higher density than the surrounding silicified wallrock breccia. Similar sulfide types may exhibit different relations between bulk density and porosity for Hole 957H (as seen in Fig. 37), because of the heterogeneous nature of the measured sulfide breccias.

#### Compressional (P-wave) Velocities

The two minicores (158-957H-5N-1, 33–35 cm, and 5N-2, 29–31 cm) exhibit compressional (*P*-wave) velocities of 5.4 and 6.7 km/s, respectively (Table 10). The difference in velocity measured in the two minicores is attributed to a 12% higher pyrite content in minicore Sample 158-957H-5N-2, 29–31 cm, compared to Sample 158-957H-5N-1, 33–35 cm (Table 2).

#### Electrical Resistivity

The same two minicore samples exhibit resistivity values of 0.584 and 0.068 Ωm, respectively (Table 10). The lower resistivity in minicore Sample 158-957H-5N-2, 29–31 cm, is attributed to the higher pyrite content and its higher porosity.

#### Thermal Conductivity

Two half-round samples (158-957H-5N-1, Piece 5A, 29–40 cm, and 5N-2, Piece 1D, 27–33 cm) from the archive halves of Core 158-957H-5N correspond to the working halves of the core where the two

Table 7 (continued).

Groundmass	Vesicle (%)	Glass (%)	Alter. (%)	Comments - crystallinity (holo/hypo/hyalo)
				Texture (seriate, poikilitic, ophitic, subophitic, intergranular, intersertal, phytic, etc.)
Glassy to microcrystalline	2	30	100	Interpillow/breccia fragments in mud (metalliferous sediments?); basalt altered to smectite; glass altered to chlorite
Glassy to microcrystalline	2	30	100	Interpillow/breccia fragments in mud (metalliferous sediments?); basalt altered to smectite; glass altered to chlorite
Glassy to microcrystalline	2	30	100	Interpillow/breccia fragments in mud (metalliferous sediments?); basalt altered to smectite; glass altered to chlorite
Glassy to microcrystalline	2	30	100	Interpillow/breccia fragments in mud (metalliferous sediments?); basalt altered to smectite; glass altered to chlorite
Glassy	2	100	100	Glass cemented by hydrothermal silica; disseminated sulfide grains present
Microcrystalline	2	0	15	Vesicles filled with smectite
Microcrystalline	2	0	7	Vesicles filled with smectite
Microcrystalline	2	0	7	Vesicles filled with smectite
Microcrystalline	0	0	100	Basalt altered to chlorite
Microcrystalline	2	0	100	Vesicles filled with smectite

Table 9. Index properties of samples recovered from Holes 957B and 957H.

Core, section, interval (cm)	Depth (mbsf)	Bulk water content (%)	Bulk density [B] (g/cm <sup>3</sup> )	Bulk density [C] (g/cm <sup>3</sup> )	Grain density [B] (g/cm <sup>3</sup> )	Grain density [C] (g/cm <sup>3</sup> )	Porosity [B] (%)	Porosity [C] (%)	Rock type (F = fragment, M = minicore)
158-957B-									
1R-1, 44-46	0.44	33.95	1.84	1.86	3.12	3.19	61.00	61.56	Fe-oxides and sulfide sand
1R-2, 12-14	1.15	8.19	2.67	2.61	3.12	3.03	21.37	20.89	Porous massive sphalerite (F)
4R-1, 17-19	20.07	8.49	2.60	2.25	3.03	2.53	21.52	18.63	Altered basalt (F)
5B-1, 1-3	29.61	6.61	2.72	2.43	3.08	2.69	17.56	15.65	Altered basalt (F)
158-957H-									
1N-1, 19-21	8.89	6.74	3.41	3.27	4.10	3.89	22.41	21.53	Porous massive pyrite (F)
2N-1, 7-9	13.27	2.33	4.38	4.02	4.75	4.32	9.96	9.13	Porous nodular pyrite breccia (F)
3N-1, 45-47	18.15	2.90	4.30	4.07	4.76	4.47	12.18	11.52	Porous nodular pyrite breccia (F)
5N-1, 33-35	27.03	2.46	3.82	3.70	4.11	3.96	9.17	8.88	Nodular pyrite-silica breccia (M)
5N-2, 29-31	27.89	2.35	4.46	4.33	4.84	4.69	10.20	9.92	Silicified wallrock breccia (M)
6N-1, 20-22	31.40	1.84	3.88	3.65	4.09	3.83	6.96	6.55	Nodular pyrite-silica breccia (F)
8N-1, 97-99	41.17	2.60	3.77	3.67	4.06	3.94	9.56	9.30	Pyrite-silica breccia (F)
9X-1, 15-17	44.85	1.80	3.76	3.63	3.95	3.81	6.60	6.38	Massive pyrite breccia (F)

Note: [B] and [C] refer to the method used to calculate bulk and grain density (see "Index Properties" section, "Explanatory Notes" chapter, this volume).

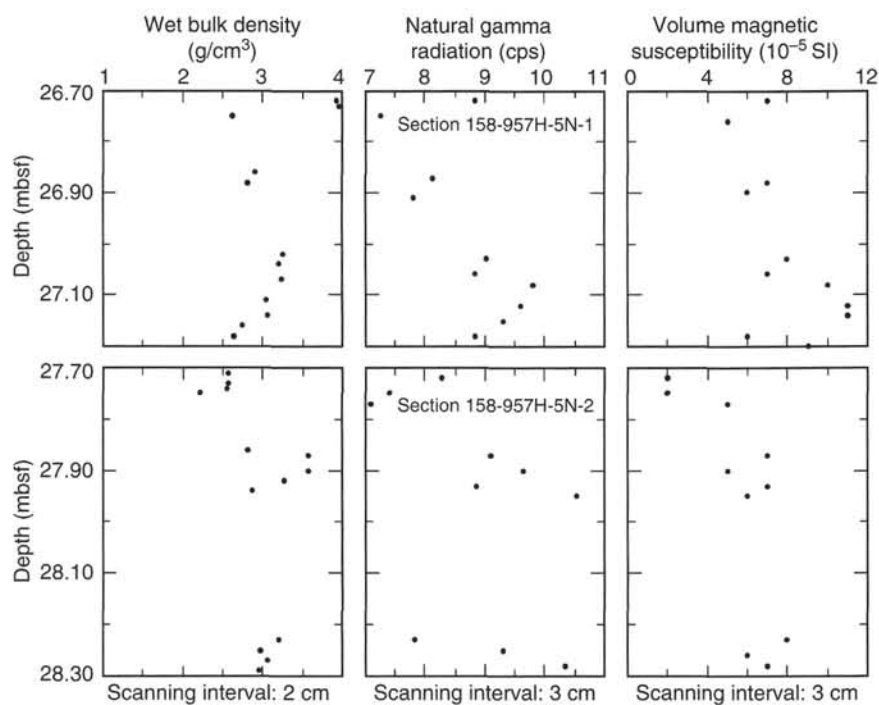


Figure 35. Results from multisensor track (MST) scans of intact intervals from Core 158-957H-5N (intervals 158-957H-5N-1, 2-49 cm, and 5N-2, 11-69 cm). The measured physical properties are uncorrected wet bulk density obtained by the GRAPE instrument, natural gamma radiation, and volume magnetic susceptibility.

minicore samples (158-957H-5N-1, 33-35 cm, and 5N-2, 29-31 cm) were extracted. The half-round samples exhibit thermal conductivities (mean of three measurements each) of 10.16 and 8.01 W/(m·K), respectively (Table 11).

Based on higher density values and lower resistivity measurements, as well as the higher pyrite content measured in minicore Sample 158-957H-5N-2, 29-31 cm, compared to minicore Sample

158-957H-5N-1, 33-35 cm, thermal conductivity would be expected to be higher in Core 158-957H-5N-2 than in Core 158-957H-5N-1. The thermal conductivities measured on the slabs in the archive half of the two cores from which the minicores were extracted proved to be opposite this expectation (Table 11). To check this apparent discrepancy, the thermal conductivity measurements on the same archive halves (Samples 158-957H-5N-1, Piece 5A, 29-40 cm, and

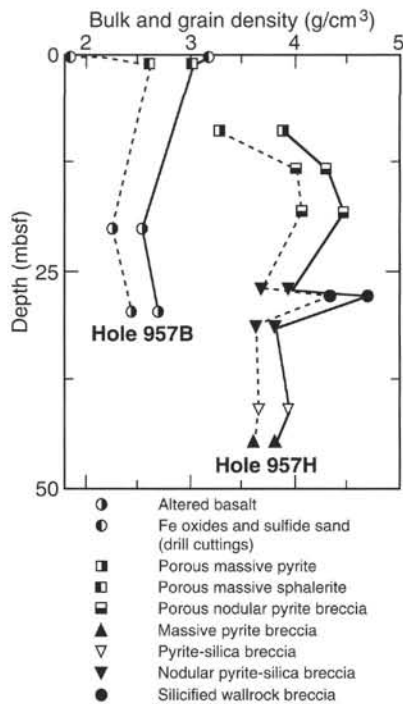


Figure 36. Bulk (dashed line) and grain (solid line) density values of samples identified by rock type vs. depth, Holes 957B and 957H.

5N-2, Piece 1D, 27–33 cm) were repeated 2 days after the initial measurements and the initial conductivity values were confirmed (mean values of 10.41 and 8.58 W/[m·K] based on five measurements each; Table 11). This apparent discrepancy is explained by the observation that thermal conductivity is measured on a half-round slab of the archive half with different bulk physical properties than the minicore extracted from the corresponding slab of the working half. In this case, the interval of the half-round slab (Sample 158-957H-5N-2, Piece 1D, 27–33 cm) is a silicified wallrock breccia, but the extracted minicore (Interval 158-957H-5N-2, 29–31 cm) represents a pyrite-rich interval within the slab.

### Summary

Nine sulfide specimens analyzed from the Kremlin area of the active TAG mound (Holes 957B and 957H) yielded a range of bulk densities (2.61–4.33 g/cm<sup>3</sup>) and porosities (6.38%–21.5%) similar to the values measured at the TAG-1 area, with no consistent relations between bulk density and porosity of the different sample types or between these parameters and depth below seafloor. However, the samples from Hole 957B showed consistently lower densities and higher porosities than those from Hole 957H. Two fragments of altered basalt exhibit a narrow range of low densities (2.25 and 2.43 g/cm<sup>3</sup>) and a narrow range of high porosities (15.65% and 18.63%).

Compressional (*P*-wave) velocities are higher (5.4 and 6.7 km/s) than in the TAG-1 area. Thermal conductivities measured on half-round slabs are slightly higher (8.0 and 10.4 W/[m·K]) than the TAG-1 area.

### PALEOMAGNETISM

Two vertically oriented archive-half sections from Hole 957H in the TAG-2 area were measured using the cryogenic magnetometer

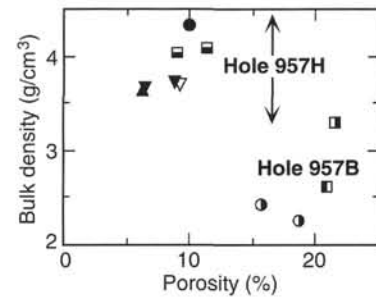


Figure 37. Bulk density vs. porosity for samples identified by rock type, Holes 957B and 957H. Symbols as in Figure 36.

and alternating-field (AF) demagnetized progressively at 10-cm intervals using peak fields of 10, 15, 20, and 25 mT. The whole-core volume magnetic susceptibility of these two sections was measured at 3-cm intervals using the automated MST. Two minicore samples were taken from Sections 158-957H-5N-1 and 5N-2, respectively, for stepwise demagnetization and rock magnetic characterization study. The NRM and the bulk magnetic susceptibility were measured to calculate the Koenigsberger ratio (see “Paleomagnetism” section, Chapter 5, this volume) of the two minicore samples. The samples were then subjected to progressive alternating-field (AF) demagnetization to a peak field of 25 mT before the anisotropy of magnetic susceptibility (AMS) for these two samples was measured. A 15-position measurement scheme was used to derive the susceptibility tensor ( $k_{ij}$ ) and associated eigenvectors and eigenvalues, using the Kappabridge and the program ANI20 supplied by Geofyzika Brno. Subsequently, the two samples were demagnetized in progressive steps of increasing AF field, up to 60 mT.

### Demagnetization Behavior

Figures 38 and 39 present the natural remanent magnetization (NRM) intensities and inclinations before and after 25 mT AF demagnetization, as observed in Core 158-957H-5N. The NRM intensity profile shows a trend of downhole increase with a standard deviation of 9.32°. A distinctive high peak in NRM intensity (Fig. 38A) occurs at about 27 mbsf, which also corresponds to a low peak (negative value!) in inclination (Fig 39A). The AF demagnetization to 25 mT successfully removed this spurious magnetization, as shown by the disappearance of both peaks as well as the significant decrease in standard deviation (1.29°). The fact that AF demagnetization to 25 mT can effectively remove this spurious magnetic signal leads us to suspect that this magnetization is perhaps related to a viscous remagnetization. With an exception around a depth of 28 mbsf where inclination is near vertical, the AF-cleaned inclination values cluster around 50°, which is the expected inclination at the drilling site. However, the trend of increasing intensity with depth still exists after 25 mT demagnetization. Average intensity for the upper section (to a depth of 27.45 mbsf) is 0.81 mA/m; for the lower section, it is 2.78 mA/m. This exponential increase in intensity coincides with changes observed in the lithology (from nodular pyrite-silica breccia in Section 158-957H-5N-1 to silicified basalt breccia in Section 158-957H-5N-2; see “Stratigraphy” section). Progressive AF demagnetization up to 60 mT on Samples 158-957H-5N-1, 33–35 cm (nodular pyrite-silica breccia), and 5N-2, 29–31 cm (silicified basalt breccia), revealed two components of magnetization (Fig. 40). The first component can be erased at the initial stage of demagnetization, indicating that it is probably of viscous origin. Subsequent demagnetization isolated a second, more stable component of magnetization. As mentioned above, the downhole inclination profile deviates radically where inclination is much steeper than the expected value. This was

**Table 10. Electrical resistance, *P*-wave velocity, and related properties measured in minicores recovered from Hole 957H.**

Core, section, interval (cm)	Depth (mbsf)	Length (mm)	Diameter (mm)	Resistance ( $\Omega$ )	Resistivity ( $\Omega\text{m}$ )	Formation factor	<i>P</i> -wave velocity (km/s)	Rock type
158-957H-5N-1, 33–35	27.03	21.48	25.27	25	0.584	2.919	5.402	Nodular pyrite-silica breccia
5N-2, 29–31	27.89	22.28	25.26	3	0.068	0.337	6.749	Silicified wallrock breccia

**Table 11. Thermal conductivity values measured on half-round sulfide samples from Hole 957H.**

Core, section, interval (cm)	Piece no.	Depth (mbsf)	Thermal conductivity (W/[m·K])	Error (W/[m·K])	Rock type
158-957H-5N-1 29–40	5A	26.99	10.16	0.012	Nodular pyrite-silica breccia
			10.41	0.009	Remeasurement of same sample
5N-2, 27–33	1D	27.87	8.01	0.011	Silicified wallrock breccia
			8.58	0.009	Remeasurement of same sample

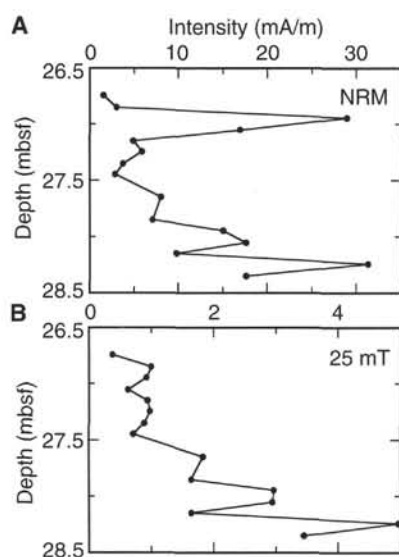


Figure 38. The downhole variation of intensity of NRM before (A) and after (B) alternating-field (AF) demagnetization at 25 mT for Core 158-957H-5N.

also observed in Sample 158-957H-5N-2, 29–31 cm (Fig. 40B). The stable inclination for this sample is 84.8°, which indicates that a nearly vertically directed, drilling-induced magnetization is probably still present in this sample. As demonstrated in demagnetization experiments on samples from Hole 957C, it appears that AF demagnetization is not sufficient to undo the acquisition of this drilling-induced magnetization.

### Rock Magnetic Properties of Minicore Samples

The operational difficulties of drilling gave us time to complete several rock magnetic measurements that are not standard procedure on ODP legs. Table 12 summarizes these measurements on two minicore samples.

#### Koenigsberger Ratio

The Koenigsberger ratio  $Q$  is defined as the ratio in a rock of remanent magnetization to magnetization induced in the Earth's field. In general, the Koenigsberger ratio is used as a measure of stability to indicate a rock's capability of maintaining a stable remanence. The IGRF field value at the TAG site (42,000 nT = 33.44 A/m) was used to calculate  $Q$ . The silicified basalt breccia in Sample 158-957H-5N-

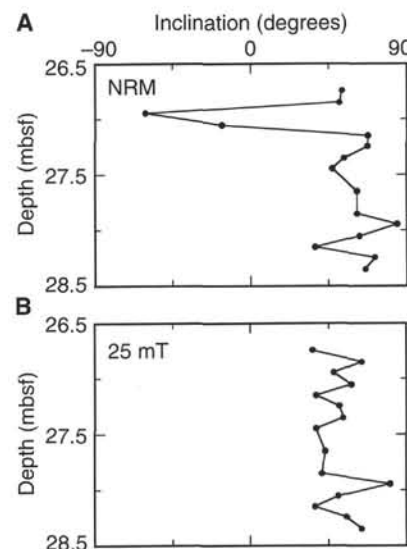


Figure 39. The downhole variation of inclination of NRM before (A) and after (B) alternating-field (AF) demagnetization at 25 mT for Core 158-957H-5N.

2, 29–31 cm, has a higher remanence intensity than the nodular pyrite-silica breccia in Sample 158-957H-5N-1, 33–35 cm; consequently, the Koenigsberger ratio of the former is higher than that of the latter. The Koenigsberger ratio for Sample 158-957H-5N-1, 33–35 cm, is slightly greater than 1.0, indicating that induced magnetization would be comparable to that of remanent magnetization. The low value of the Koenigsberger ratio for this sample also indicates the presence of low-coercivity magnetic minerals, which carry an unstable remanence and are more susceptible to an external magnetic field. This is indeed reflected in the magnetic susceptibility data: the susceptibility of this sample is substantially higher than that of Sample 158-957H-5N-2, 29–31 cm (see Table 12 for these values and discussion below).

#### Magnetic Susceptibility

The low-field susceptibility values listed in Table 12 were obtained using two different instruments in the ship's paleomagnetic lab, which yielded overlapping results. These values are also in full agreement with the downhole profile of magnetic susceptibility for Core 158-957H-5N (Fig. 41). The downhole magnetic susceptibility profile shows a trend of decreasing susceptibility with depth, a trend that is opposite in sense to that of the downhole NRM intensity profile. Within the top 27 m, which corresponds to the nodular pyrite-silica

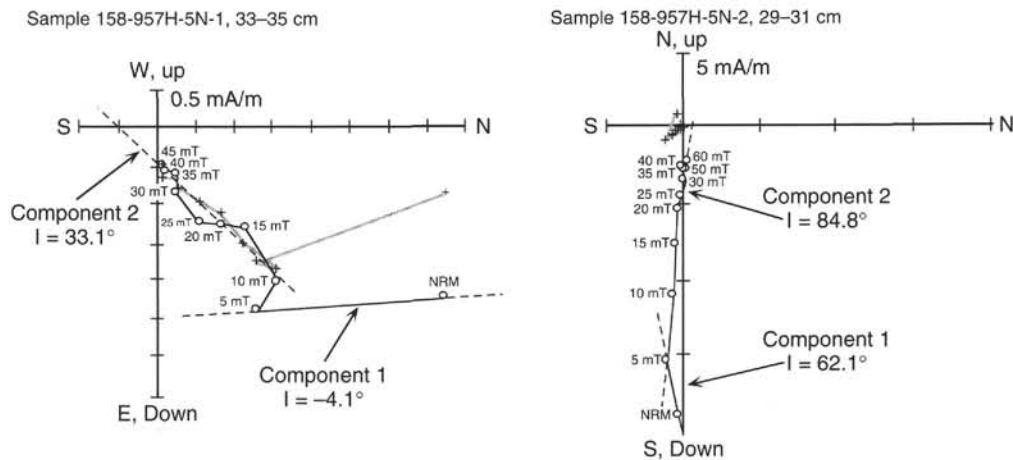


Figure 40. Vector endpoint diagram showing the results of alternating-field demagnetization for discrete samples from Cores 158-957H-5N. The magnetic component is shown by a straight dashed line fitting the data points and the corresponding inclination ( $I$ ) is indicated. Open circles and crosses represent vector endpoints projected onto the vertical and horizontal planes, respectively.

Table 12. Magnetic properties of minicore samples from Hole 957H.

Core, section, interval (cm)	Depth (mbsf)	NRM intensity (mA/m)	Declination (degrees)	Inclination (degrees)	K ( $10^{-6}$ SI)	Q ratio	$P = K_1/K_3$
158-957H-5N-1, 33-35	27.03	4.46	41.1	33.1	84.13	1.585	1.050
5N-2, 29-31	27.89	19.1	252.7	84.8	65.13	8.770	1.051

Notes: Inclination = stable inclination after demagnetization; K = magnetic susceptibility in  $10^{-6}$  SI units; Q ratio = Koenigsberger ratio; P = anisotropy factor;  $K_1$  and  $K_3$  = maximum and minimum principal axes of susceptibility.

breccia unit in Section 158-957H-5N-1, the magnetic susceptibilities have values that are consistently above  $5 \times 10^{-5}$  SI units. A susceptibility maximum occurs at about 27 mbsf, which corresponds to the high peak in NRM intensity curve (Fig. 38A). As described earlier, this high peak can be removed by 25 mT AF demagnetization and is probably caused by unstable viscous remanence. This information is in agreement with the observed lower Koenigsberger ratio in this section. The susceptibility values decrease below 27.5 mbsf (to a mean value  $4.61 \times 10^{-5}$  SI units) in the silicified basalt breccia unit of Section 158-957H-5N-2, which also displayed a higher Koenigsberger ratio. Thus, magnetic measurements from the two sections in Hole 957H indicate that higher magnetic susceptibility values could arise from unstable viscous remanence with a lower Koenigsberger ratio.

#### Anisotropy of Magnetic Susceptibility (AMS)

Anisotropy of magnetic susceptibility (AMS) is a physical property of rocks that is used for petrofabric and structural studies. It measures the sum of the anisotropies of the individual minerals in a rock. AMS results can be described by an ellipsoid of magnetic susceptibility, with dimensions defined by the magnitudes of the principal susceptibilities. These lie along the three orthogonal axes of the ellipsoid and are designated the maximum, intermediate, and minimum susceptibilities ( $K_1$ ,  $K_2$ , and  $K_3$ , respectively). These quantities are combined in various ways to describe different features of the ellipsoid and of the magnetic fabric it represents. AMS in massive sulfides likely arises from the preferred orientation of anisotropic magnetic minerals. It is probable that net preferred alignment can be enhanced in these rocks by hydrothermal alteration. The ratio  $K_1/K_3$  (P in Table 12) is commonly used as a measure of the degree of anisotropy. In the two samples studied, this ratio is very low (1.015 for both samples), indicating that virtually no anisotropy is present in the samples. The

AMS results suggest that these samples were probably not under a strong stress-field during formation.

In summary, the cores recovered from Hole 957H in the Kremlin area display a multicomponent magnetization. The unstable viscous component is characterized by higher magnetic susceptibility and lower Koenigsberger ratio. This viscous magnetization can be removed by AF demagnetization. The downhole magnetic profile shows a trend of increasing intensity with depth, which coincides with changes observed in the lithology. No noticeable magnetic anisotropies were observed in cores from Hole 957H.

## FLUID GEOCHEMISTRY

Bottom water was collected using the WSTP, triggered in the vicinity of Hole 957A approximately 2.5 m above the seafloor, near marker float number 7C. The sample retrieved (WSTP-1) included 10 mL contained in the titanium tube and 1 L contained in the overflow chamber.

### Results

Table 13 provides a summary of dissolved constituents determined by shipboard analyses. The salinity measured for bottom water near Hole 957A is typical of North Atlantic Deep Water, that is, 34.9‰ (Sverdrup et al., 1942). Dissolved phosphate and silica are within the ranges expected for normal bottom water (Broecker and Peng, 1982; Redfield et al., 1982). We see no evidence in the shipboard chemical analyses to suggest the presence of a hydrothermal component in the bottom-water sample.

Equilibrium temperature determined by WSTP was 5.4°C. When compared to bottom-water temperatures between 2.65° and 2.71°C measured during Alvin dives to the TAG mound (Becker and Von

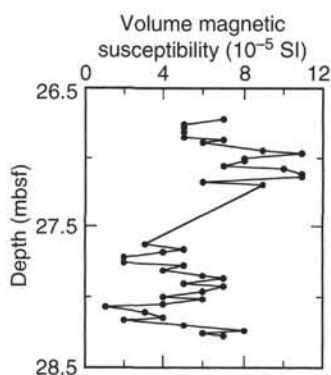


Figure 41. Plot of magnetic susceptibility as a function of depth in Hole 957H, showing that the whole-core susceptibility measurements vary in opposite fashion to the NRM signals, with a mean value of  $7.64 \times 10^{-5}$  SI units for Section 158-957H-5N-1 (depth interval 26.72–27.20 mbsf) and  $4.61 \times 10^{-5}$  SI units for Section 158-957H-5N-2 (depth interval 27.62–28.28 mbsf).

Herzen, this volume), the WSTP temperature is high. In the absence of chemical evidence supporting the presence of hydrothermal fluids in the WSTP-1 sample, we interpret the WSTP temperature to be an artifact of calibration and not the true bottom-water temperature.

## REFERENCES

- Broecker, W.S., and Peng, T.-H., 1982. *Tracers in the Sea*: Palisades, NY (Lamont-Doherty Geological Observatory).
- Deer, W.A., Howie, R.A., and Zussman, J., 1966. *An Introduction to the Rock-Forming Minerals*: London (Longman Group).
- Edmond J.M., Campbell, A.C., Palmer, M.R., German, C.R., Klinkhammer, G.P., Edmonds, H.N., Elderfield, H., Thompson, G., and Rona, P., 1995. Time series studies of vent fluids from the TAG and MARK sites (1986, 1990): Mid-Atlantic Ridge: a new solution chemistry model and a mechanism for Cu/Zn zonation in massive sulfide ore bodies. In Parson, L.M., Walker, C.L., and Dixon, D.R. (Eds.), *Hydrothermal Vents and Processes*. Geol. Soc. Spec. Publ. London, 87:77–86.
- Redfield, A.C., Ketchum, B.H., and Richards, F.A., 1982. The influence of organisms on the composition of seawater. In Hill, M.N. (Ed.), *The Sea* (Vol. 2): New York (Wiley), 26–49.
- Sverdrup, H.U., Johnson, M.W., and Fleming, R. (Eds.), 1942. *The Oceans: Their Physics, Chemistry and General Biology*: Englewood Cliffs, NJ (Prentice-Hall).
- Tivey, M.K., Humphris, S.E., Thompson, G., Hannington, M.D., and Rona, P.A., 1995. Deducing patterns of fluid flow and mixing within the TAG active hydrothermal mound using mineralogical and geochemical data. *J. Geophys. Res.*, 10:12527–12555.

Ms 158IR-108

**NOTE: For all sites drilled, core-description forms (“barrel sheets”) and core photographs can be found in Section 3, beginning on page 227. Thin-section data are given in Section 4, beginning on page 345.**

**Table 13. Dissolved ion concentrations in surface seawater, bottom water, and borehole fluids in Holes 957A and 957C, and typical values expected for natural waters in the vicinity of Site 957.**

Sample	Water depth (m)	pH	Alkalinity (mmol/L)	Salinity (‰)	K <sup>+</sup> (mmol/L)	Mg (mmol/L)	Ca <sup>2+</sup> (mmol/L)	Cl <sup>-</sup> (mmol/L)	SO <sub>4</sub> <sup>2-</sup> (mmol/L)	PO <sub>4</sub> (μmol/L)	NH <sub>3</sub> (μmol/L)	SiO <sub>2</sub> (μmol/L)
157-957A-Surface water	0	8.21	2.56	36.5	11.1	55.9	11.1	583	31.6	<0.1	3	<10
WSTP-1	3648.5	7.52	2.33	34.9	10.5	54.4	10.3	544	30.1	1	29	33
157-957C-WSTP-2	3648	7.7	2.49	35	10.7	54.5	10.2	543	28.1	1.7	31	57
Sample	Depth (m)	pH	Alkalinity (mmol/L)	Salinity (‰)	K <sup>+</sup> (mmol/L)	Mg (mmol/L)	Ca <sup>2+</sup> (mmol/L)	Cl <sup>-</sup> (mmol/L)	SO <sub>4</sub> <sup>2-</sup> (mmol/L)	PO <sub>4</sub> (μmol/L)	NH <sub>3</sub> (μmol/L)	SiO <sub>2</sub> (μmol/L)
158-957C-10N-1, 10-15	28.65	8.02	2.53	38.5	11.4	58.4	17.7	587	42.5	<0.1	32	4
NASW				36.5–37 (S)						<1 (R)		<10 (B)
NADW				34.9 (S)						1–1.5 (R)		20–40 (B)

Notes: NASW = North Atlantic surface water, and NADW = North Atlantic Deep Water. (S) = from Sverdrup et al. (1942), (R) = from Redfield et al. (1982), and (B) = from Broecker and Peng (1982).